CrossMark

JℳM PAPERS

Direct numerical simulations of turbulent pipe flow up to $Re_\tau \approx 5200$

Jie Yao[1], Saleh Rezaeiravesh[2], Philipp Schlatter[2] and Fazle Hussain[1],†

[1]Department of Mechanical Engineering, Texas Tech University, Lubbock, TX 79409, USA

[2]Department of Engineering Mechanics, KTH Royal Institute of Technology, SE-100 44 Stockholm, Sweden

Well-resolved direct numerical simulations (DNS) have been performed of the flow in a smooth circular pipe of radius R and axial length $10\pi R$ at friction Reynolds numbers up to $Re_\tau = 5200$ using the pseudo-spectral code OPENPIPEFLOW. Various turbulence statistics are documented and compared with other DNS and experimental data in pipes as well as channels. Small but distinct differences between various datasets are identified. The friction factor λ overshoots by 2 % and undershoots by 0.6 % the Prandtl friction law at low and high Re ranges, respectively. In addition, λ in our results is slightly higher than in Pirozzoli *et al.* (*J. Fluid Mech.*, vol. 926, 2021, A28), but matches well the experiments in Furuichi *et al.* (*Phys. Fluids*, vol. 27, issue 9, 2015, 095108). The log-law indicator function, which is nearly indistinguishable between pipe and channel up to $y^+ = 250$, has not yet developed a plateau farther away from the wall in the pipes even for the $Re_\tau = 5200$ cases. The wall shear stress fluctuations and the inner peak of the axial turbulence intensity – which grow monotonically with Re_τ – are lower in the pipe than in the channel, but the difference decreases with increasing Re_τ. While the wall value is slightly lower in the channel than in the pipe at the same Re_τ, the inner peak of the pressure fluctuation shows negligible differences between them. The Reynolds number scaling of all these quantities agrees with both the logarithmic and defect-power laws if the coefficients are properly chosen. The one-dimensional spectrum of the axial velocity fluctuation exhibits a k^{-1} dependence at an intermediate distance from the wall – also seen in the channel. In summary, these high-fidelity data enable us to provide better insights into the flow physics in the pipes as well as the similarity/difference among different types of wall turbulence.

Key words: pipe flow, turbulence simulation, turbulent boundary layers

† Email address for correspondence: fazlehussain@gmail.com

J. Yao, S. Rezaeiravesh, P. Schlatter and F. Hussain

1. Introduction

Turbulent flows that are constrained by a wall (referred to as 'wall turbulence') are common in nature and technology. Roughly half of the energy spent in transporting fluids through pipes or vehicles through air or water is dissipated by the turbulence near the walls (Jiménez 2012). Therefore, an improved understanding of the underlying physics of these flows is essential for modelling and control (Kim 2011; Canton *et al.* 2016; Yao, Chen & Hussain 2018). The spatially evolving boundary layer, the (plane) channel and the pipe are three canonical geometrical configurations of wall turbulence. Different from boundary layer and channel flows, azimuthal periodicity is inherent to pipe flows. Therefore, pipe flow is the most canonical case, being completely described by the Reynolds number (*Re*) and the axial length – the effect of the latter is limited if sufficiently large (El Khoury *et al.* 2013; Feldmann, Bauer & Wagner 2018).

Sustained interest in high-*Re* wall turbulence stems from numerous open questions regarding the scaling of turbulent statistics, as reviewed in Marusic *et al.* (2010*b*) and Smits, McKeon & Marusic (2011*b*). For example, a characteristic of high-*Re* wall turbulence is the logarithmic law in the mean velocity with an important parameter, namely the von Kármán constant κ, whose value and universality among different flow geometries are still highly debated (Nagib & Chauhan 2008; She, Chen & Hussain 2017). Also, there is no consensus on whether the near-wall peak of the streamwise velocity fluctuations increases continuously with *Re* (Marusic, Baars & Hutchins 2017) or eventually saturates at high *Re* (Chen & Sreenivasan 2021; Klewicki 2022). Furthermore, the existence of an outer peak in the streamwise velocity fluctuations, as indicated by experiments, is also highly debated (Hultmark *et al.* 2012; Willert *et al.* 2017). Other questions, which can be answered only with substantially higher *Re* values, concern the scaling and generation mechanism of the various flow structures. Large-scale motions (LSMs) and very-large-scale motions (VLSMs), with lengths 5*R* up to 20*R*, have been found experimentally in the outer region of pipe flows (Kim & Adrian 1999; Monty *et al.* 2007). Here, *R* is the radius of the pipe. Due to the increasing strength of these structures with *Re*, they have a footprint quite close to the wall (Monty *et al.* 2007), in the form of amplitude modulation as reviewed by e.g. Dogan *et al.* (2018).

Fundamental studies of wall turbulence require accurate representations or measurements of the flows, which were typically carried out via experiments (Zagarola & Smits 1998; McKeon, Zagarola & Smits 2005; Smits *et al.* 2011*a*; Furuichi *et al.* 2015, 2018; Talamelli *et al.* 2009; Fiorini 2017). However, decades of experimental research have shown that obtaining unambiguous high-*Re* data, particularly near the wall, remains a challenge. This is because the smallest scales decrease with increasing *Re* – leading to large uncertainties in determining the probe locations and turbulence intensities. Advances in computer technology (in both hardware and software) have enshrined direct numerical simulations (DNS) as an essential tool for turbulence research. Although only moderate *Re* can be achieved at the current stage, DNS provide extensive, detailed data compared to experiments – even close to the walls where experimental data are very difficult to obtain. One of the earliest DNS for wall turbulence were performed by Kim, Moin & Moser (1987) for the channel flow at friction Reynolds number Re_τ ($\equiv u_\tau h/\nu$) ≈ 180 (here, u_τ is the friction velocity, h is the half-channel height, and ν is the fluid kinematic viscosity). They found good agreement between DNS and experimental data of Hussain & Reynolds (1975), except in the near-wall region. The discrepancy was speculated to be caused by the inherent near-wall hot-wire measurement errors. Eggels *et al.* (1994) subsequently conducted the

first DNS of pipe flow at $Re_\tau \approx 180$ to investigate the differences between channel and pipe flows.

Numerous DNS investigations have been carried out in the aftermath of these pioneering studies, with *Re* increasing progressively as a result of increased computational power (Moser, Kim & Mansour 1999; Wu & Moin 2008; Bernardini, Pirozzoli & Orlandi 2014). However, among them, only those with $Re_\tau \geq 10^3$ are of particular engineering interest as this is the range of *Re* relevant to industrial applications. Also, it is in this range that the high-*Re* characteristics of wall turbulence start to manifest. One of the highest Re_τ large-domain DNS was performed by Lee & Moser (2015) for channel flows at $Re_\tau = 5186$ with domain size $L_x \times L_z = 8\pi h \times 3\pi h$. Compared to numerous DNS for channel flows (Bernardini *et al.* 2014; Lozano-Durán & Jiménez 2014; Lee & Moser 2015), fewer high-*Re* studies have addressed pipe flow, and most of them are limited to $Re_\tau \approx 1000$. For example, Lee & Sung (2013) performed DNS at $Re_\tau \approx 1000$ with length $30R$ and established the existence of VLSMs of scale up to $O(20R)$. El Khoury *et al.* (2013) used a spectral-element method to perform DNS for Re_τ up to 1000 with length $L_z = 25R$. Chin, Monty & Ooi (2014) found that the mean velocity profile does not exhibit a strictly logarithmic layer with Re_τ up to 2000, necessitating a finite-*Re* correction like those introduced by Afzal (1976) and Jiménez & Moser (2007). To quantify the effects of computational length and *Re*, Feldmann *et al.* (2018) conducted DNS for $90 \leq Re_\tau \leq 1500$ with L_z up to $42R$. They confirmed that $L_z = 42R$ is sufficiently large to capture the LSM- and VLSM-relevant scales. Ahn *et al.* (2015) performed DNS of pipe flow at $Re_\tau \approx 3000$ for length $30R$. They claimed that the mean velocity follows a power law in the overlap region, and observed a clear scale separation between inner- and outer-scale turbulence. So far, the largest DNS of pipe flow have been done at $Re_\tau \approx 6000$ with a relatively short length ($L_z = 15R$) by Pirozzoli *et al.* (2021) based on a lower-order numerical method.

In general, one expects various simulations and experiments to agree with each other to a high degree. However, a comparison among several datasets in spatially developing turbulent boundary layers (Schlatter & Örlü 2010), channels (Lee & Moser 2015) and pipes (Pirozzoli *et al.* 2021) shows, surprisingly, considerable variations among the various DNS, even for basic measures such as the shape factor, the friction coefficient and the von Kármán constant. Accurate turbulence statistics are very much needed, both for understanding turbulence physics and for developing, adapting and validating turbulence models. Here, we present a new high-fidelity DNS dataset of turbulent pipe flow generated with a pseudo-spectral method for Re_τ up to 5200 and with axial length $L_z/R = 10\pi$, which is long enough to capture the LSMs and VLSMs reported in experimental studies (Guala, Hommema & Adrian 2006). The accuracy of this dataset is quantified by using the newly developed uncertainty quantification method. In addition, the dataset is compared extensively with other DNS and experimental data for turbulent pipe and channel flows.

2. Simulation details

DNS of incompressible turbulent pipe flows are performed using the pseudo-spectral code 'OPENPIPEFLOW' developed by Willis (2017). The radial, axial and azimuthal directions are represented by r, z and θ, and the corresponding velocity components are u_r, u_z and u_θ. In the periodic axial (z) and azimuthal (θ) directions, Fourier discretization is employed, and the numbers of Fourier modes in the z- and θ-directions are N_z and N_θ, respectively. Note that in the physical space, the numbers of grid points in the z- and θ-directions increase by a factor $3/2$ due to dealiasing. In the radial (r) direction, a

Re_τ	Re_b	$N_z \times N_r \times N_\theta$	Δz^+	Δr_w^+	Δr_{max}^+	$\Delta(R\theta)^+$	Tu_τ/R	Symbols
181	5300	$1024 \times 192 \times 256$	5.5	0.02	2.0	4.4	105.3	⊟
549	19,000	$2048 \times 256 \times 768$	8.4	0.09	3.2	4.5	24.7	⊖
998	37700	$3072 \times 384 \times 1280$	10.2	0.1	3.9	4.9	17.1	▽
2001	83000	$6144 \times 768 \times 2560$	10.2	0.1	3.9	4.9	9.7	△
5197	240000	$12288 \times 1024 \times 5120$	12.8	0.2	8.6	6.3	4.6	☆

Table 1. Summary of simulation parameters. The axial length of the pipe (L_z) is $10\pi R$, with R being the pipe radius. Here, $Re_\tau (\equiv u_\tau R/\nu)$ and $Re_b (\equiv 2U_b R/\nu)$ are the frictional and bulk Reynolds numbers, respectively; N_z and N_θ are the number of dealiased Fourier modes in the axial and azimuthal directions, and N_r is the number of grid points in the radial direction; Δz and $\Delta(R\theta)$ are the grid spacings in the axial and azimuthal directions, defined in terms of the Fourier modes. In the radial direction, Δr_w^+ represents the grid spacing at the wall, and Δr_{max}^+ denotes the maximum grid spacing. Also, Tu_τ/R is the total eddy-turnover time without the initial transient phase.

central finite difference scheme with a nine-point stencil is adopted. With this, the first- and second-order derivatives are, respectively, calculated to 8th and 7th order, which is reduced while approaching the boundaries. The grid points are distributed according to a hyperbolic tangent function so that high wall-normal velocity gradients in the viscous sublayer can be resolved. In addition, the first few points near $r = 0$ are also clustered to preserve the high order of the finite difference scheme across the pipe axis. No-slip and no-penetration boundary conditions are enforced at the wall (i.e. $r/R = 1$), where an actual grid point is located. To avoid numerical singularity, there is no grid point at $r = 0$; and the boundary conditions on the extrapolated fields are specified based on symmetry. In particular, given a Fourier mode with azimuthal index m, each mode is odd/even if m is odd/even for u_z and p, and each mode is even/odd if m is odd/even for u_r and u_θ. The governing equations are integrated with a second-order semi-implicit time-stepping scheme. The flow is driven by a pressure gradient, which varies in time to ensure that the mass flux through the pipe remains constant. For more details about the code and the numerical methods, see Willis (2017).

Five different Reynolds numbers, $Re_\tau \approx 180$, 550, 1000, 2000, and 5200, are considered. The detailed simulation parameters, such as domain sizes and grid sizes, are listed in table 1. The simulations are performed with resolutions comparable to those used in the prior simulations, e.g. Lozano-Durán & Jiménez (2014) and Lee & Moser (2015). In particular, for $Re_\tau \leq 2000$, the axial and azimuthal resolutions employed here satisfy the criterion suggested by Yang *et al.* (2021) for capturing 99 % of the wall shear stress events. For the highest Re_τ case (i.e. ≈ 5200), $N_z = 12288$ and $N_\theta = 5120$ Fourier modes are used in the z- and θ-directions – corresponding to an effective resolution $\Delta z^+ = L_x^+/N_z = 12.8$ and $\Delta(R\theta)^+ = (2\pi R^+)/N_\theta = 5.1$. Hereinafter, the superscript + indicates non-dimensionalization in wall units, i.e. with kinematic viscosity ν and friction velocity u_τ. Along the radial direction, the minimum and maximum grid spacings in wall units are 0.2 and 8.6, respectively. Additional information on this highest Re_τ simulation is provided in Appendix A.

For comparison, several DNS and experimental data from the literature are included. The details are listed in table 2. To further validate the accuracy of our simulation, an additional simulation at $Re_\tau = 2000$ is performed using NEK5000 (hereinafter, this case is denoted as NEK5000 2K). The numerical set-up and mesh generation are the same as those in El Khoury *et al.* (2013). The length of the pipe is chosen as $L_z = 35R$, and the total number of spectral elements is 7598080. With the polynomial order set to 12, the

Reference	Type	Method	Re_τ	L_z/R	Δz^+	Δr_w^+	Δr_{max}^+	$\Delta(R\theta)^+$
Wu & Moin (2008)	DNS	FD	180	15	5.31	0.167	1.647	2.22
			1140		8.37	0.41	11.3	7.01
El Khoury et al. (2013)	DNS	SE	180	30	(3.03, 9.91)	0.14	4.44	(1.51, 4.93)
			550		(3.06, 9.99)	0.15	4.49	(1.45, 4.75)
			1000		(2.01, 9.98)	0.15	5.12	(0.98, 4.87)
Chin et al. (2014)	DNS	SE	180	20π	6.7	0.5	3.6	8.4
			550	8π	6.8	0.07	5.5	8.2
			1002	8π	7.87	0.6	7.3	6.56
			2003	3π	9.22	0.35	8.2	7.6
Ahn et al. (2013, 2015)	DNS	FD	180	30	5.25	0.165	1.628	2.2
			544		8.02	0.176	4.28	6.72
			934		6.84	0.334	9.244	5.73
			3008		7.34	0.36	9.91	6.15
Pirozzoli et al. (2021)	DNS	FD	180	15	10.54	0.027	3.89	4.41
			495		9.66	0.027	4.8	4.06
			1137		9.51	0.025	5.64	3.98
			1976		9.64	0.026	6.62	4.03
			3028		9.85	0.027	7.48	4.12
			6019		9.79	0.026	8.82	4.1
Furuichi et al. (2015, 2018)	EXP	LDV	1000–53 000	—	—	—	—	—
Lee & Moser (2015)	DNS (channel)	SB	180	8π	4.5	0.074	3.4	3.1
			544		8.9	0.019	4.5	5.0
			1000		10.9	0.019	6.2	4.6
			1995		12.2	0.017	8.2	6.1
			5186		12.7	0.498	10.3	6.4
Hoyas et al. (2022)	DNS (channel)	SC	10 000	2π	15.3	0.3	12	7.6

Table 2. List of references of data used. FD denotes (second order) finite difference, SE denotes spectral element, SB denotes spectral/B-spline, SC denotes spectral/compact finite difference, and LDV represents laser Doppler velocimetry. L_z is the axial (streamwise) length, Δz and $\Delta(R\theta)$ are the grid spacing in the axial and azimuthal directions, defined in terms of the Fourier modes. In the radial direction, Δr_w^+ represents the grid spacing at the wall, and Δr_{max}^+ denotes the maximum grid spacing.
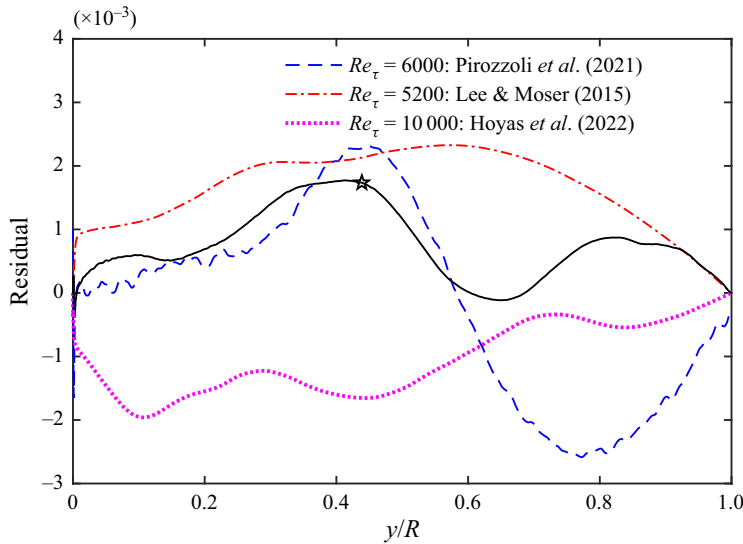
Figure 1. Comparison of the residual in the mean momentum equation (2.1) among different high-*Re* simulations. The black solid line with a star denotes our $Re_\tau = 5200$ result.

total number of grid points is approximately 13.1×10^9. The grid spacing is comparable to that used in El Khoury *et al.* (2013) in all directions.

The uncertainty in the flow quantities due to the finite time-averaging is estimated using the methods described in Rezaeiravesh *et al.* (2022) and D. Xavier *et al.* (personal communication 2022). For the central moments of velocity and pressure, the central limit theorem is applied to the time samples averaged over the z- and θ-directions. The associated time-averaging uncertainty is estimated using an autoregressive-based model for the autocorrelation function; see e.g. Oliver *et al.* (2014). For estimating the uncertainty in the combination of central moments, the method proposed by Rezaeiravesh *et al.* (2022) is employed. See Appendix B for further discussion on the method and estimated uncertainties in the first- and second-order velocity moments. For the $Re_\tau \approx 5200$ case, the estimated standard deviation of the mean axial velocity (U^+) is less than 0.1 %, and the estimated standard deviation of the velocity variance (i.e. $\langle u_r'^2 \rangle^+$, $\langle u_\theta'^2 \rangle^+$, $\langle u_z'^2 \rangle^+$) and covariance ($\langle u_r' u_z' \rangle^+$) is less than 1 % in the near-wall region ($y^+ < 100$), and approximately 5 % in the core region. Hereinafter, the velocity fluctuations are denoted using the prime symbol (e.g. u_r'), and the ensemble (in both time and space) averaged quantities are expressed using a capital letter or bracket (e.g. U or $\langle u_r' u_\theta' \rangle$).

In addition, the mean momentum equation is employed to ensure that the simulation is statistically stationary. Due to momentum balance, the total stress, which is the sum of Reynolds shear stress $\langle u_r' u_\theta' \rangle^+$ and mean viscous stress $\partial U^+/\partial y^+$, is linear in a statistically stationary turbulent pipe flow:

$$\frac{\partial U^+}{\partial y^+} - \langle u_r' u_\theta' \rangle^+ = 1 - y/R, \tag{2.1}$$

where $y = R - r$. Figure 1 shows the residual in (2.1) for the $Re_\tau \approx 5200$ case. The discrepancy between the analytic linear profile (i.e. $1 - y/R$) and total stress profile (i.e. $\partial U^+/\partial y - \langle u_r' u_\theta' \rangle^+$) from the simulation is less than 0.002 in wall units and is comparable

956 A18-6

to other high-*Re* DNS in the literature. Note that this discrepancy is much smaller than the standard deviation of the estimated total stress (see Appendix B).

3. Results

3.1. *Flow visualization*

The *Re* effect on the flow structure is illustrated qualitatively in figure 2, showing cross-sectional views of the instantaneous axial velocity u_z. Although large scales dominate in the central region of the pipe for all Re_τ cases, there is a general increase in the range of scales with increasing Re_τ. The average spacing between near-wall low-speed streaks is around $(R\theta)^+ = 100$. For the lowest Re_τ studied here, approximately ten evenly distributed low-speed structures are seen in figure 2(*a*), identified by the plume-shaped black regions ejecting from the wall. For our highest Re_τ, the streak spacing is reduced to approximately $0.02R$, and these fine-scale streaks can hardly be identified from the full cross-section in figure 2(*e*). A zoomed-in view of the near-wall region with domain size $(1000, 200)$ in wall units in (r, θ) directions is provided to better visualize these structures, which share patterns quite similar to those in low Re_τ cases.

Figures 2(*f*,*g*) show the inner-scaled instantaneous axial velocity fluctuations u'_z/u_τ on an unrolled cylindrical surface $(z - r\theta)$ for $Re_\tau \approx 5200$ at $y^+ = 15$ and $y/R = 0.5$, respectively. At $y^+ = 15$, u'_z/u_τ shows the organization of the streaks, whose characteristics are better illustrated in a zoomed-in view with domain size $(2000, 400)$ in wall units. Consistent with previous findings (Hellström, Sinha & Smits 2011; Bernardini *et al.* 2014), the flow in the outer region exhibits very long positive/negative u'_z/u_τ patches – indicating the presence of LSMs and VLSMs.

3.2. *Friction factor*

The mean friction (or wall shear stress), which is proportional to the pressure drop or the amount of energy required to sustain the flow, is an important parameter and has been studied extensively (Blasius 1913; McKeon *et al.* 2005; Furuichi *et al.* 2015; Pirozzoli *et al.* 2021). A semi-empirical relation between the friction factor $\lambda = 8\tau_{z,w}/(\rho U_b^2)$ and *Re* is given as (known as the Prandtl friction law)

$$1/\lambda^{1/2} = A \log_{10}(Re_b \, \lambda^{1/2}) - B, \tag{3.1}$$

where the constant *A* is related to the von Kármán constant as $A = 1/(2\kappa\sqrt{2}\log_{10}(e))$. Curve-fitting the experimental data over $3.1 \times 10^3 < Re_b < 3.2 \times 10^6$ by Nikuradse (1933) yields $A = 2.0$ and $B = 0.8$, which corresponds to $\kappa = 0.407$. However, notable deviations were observed when comparing the Prandtl friction law with other experimental data. For example, McKeon *et al.* (2005) showed that for the Princeton Superpipe data (in the range $3.1 \times 10^4 \leq Re_b \leq 3.5 \times 10^7$), the constants of the Prandtl law work only over a limited range of Re_b. New constants (i.e. $A = 1.920$ and $B = 0.475$) and additional *Re*-dependent corrections are needed to better fit the data in the entire Re_b range. For the 'Hi-Reff' data, Furuichi *et al.* (2015) found that λ deviates from the Prandtl law by approximately 2.5 % in the lower Re_b region, and -3 % in the high Re_b region. In addition, λ, although agreeing with the Superpipe data in the low Re_b range, deviates for $Re_b > 2 \times 10^5$.

Figure 3(*a*) shows the friction factor λ as a function of Re_b, along with other DNS and experimental data as well as the theoretical prediction λ_p based on (3.1). Note that these DNS results are conducted with various domain sizes, and prior studies demonstrated that
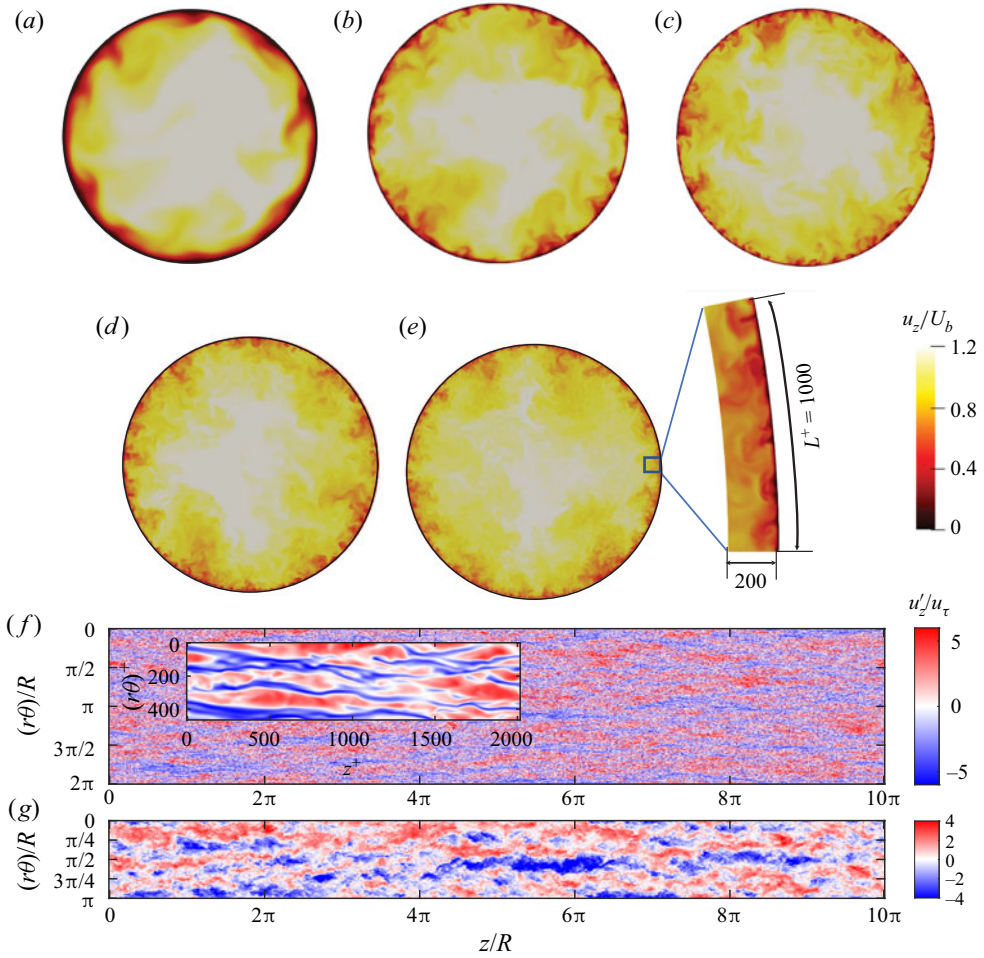
Figure 2. Visualization of the instantaneous axial velocity u_z/U_b in the (r, θ) plane for Re_τ values (a) 180, (b) 550, (c) 1000, (d) 2000, and (e) 5200; and inner-scaled instantaneous axial velocity fluctuations u_z'/u_τ on a cylindrical surface $(z - r\theta)$ for $Re_\tau = 5200$ at (f) $y^+ = 15$ and (g) $y/R = 0.5$.
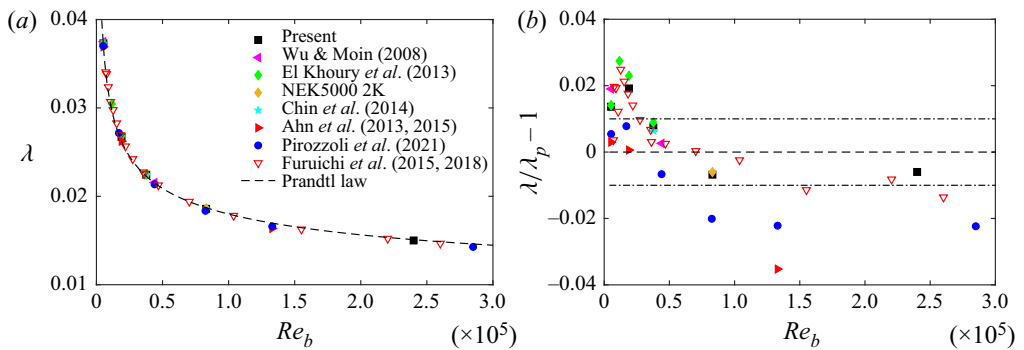

Figure 3. (a) Friction factor λ as a function of Re_b, and (b) the relative deviations from the Prandtl friction law.

its effect on one-point statistics appears limited when $L_z/R \geq 7$ (Feldmann *et al.* 2018; Pirozzoli *et al.* 2021). All DNS and experimental data seem to follow λ_p. However, the scatter is better highlighted by examining the relative error with respect to the Prandtl law (i.e. $\lambda/\lambda_p - 1$). As depicted in figure 3(*b*), all DNS data overshoot λ_p at the low Re_b (i.e. $\leq 4 \times 10^4$). Our data, which agree with Wu & Moin (2008), El Khoury *et al.* (2013) and Chin *et al.* (2014) and the new simulation at $Re = 2000$ using NEK5000, exceed λ_p by approximately 2 %, while the results of Ahn *et al.* (2013) and Pirozzoli *et al.* (2021) are closer to λ_p (within 1 % for $Re_b < 5 \times 10^4$). Pirozzoli *et al.* (2021) attributed this discrepancy to the different grid resolutions employed in the θ-direction, which is $(R\theta)^+ = 4$–5 in theirs and Ahn *et al.* (2013), but 7–8 for Wu & Moin (2008) and Chin *et al.* (2014). However, the data from El Khoury *et al.* (2013) and our DNS have azimuthal resolutions comparable to those in Ahn *et al.* (2013) and Pirozzoli *et al.* (2021), but produce results similar to Wu & Moin (2008) and Chin *et al.* (2014) – suggesting that the azimuthal resolution is not the main reason for such discrepancy. Interestingly, the data of Ahn *et al.* (2013) and Pirozzoli *et al.* (2021) are consistently lower than our and other results in the whole Re_b range. In particular, at the highest Re_b, the Pirozzoli *et al.* (2021) data undershoot by 2 % from λ_p, but our data are lower by only approximately 0.6 %. Table 3 asserts that such differences in λ are beyond the uncertainty limit.

Our DNS and the experimental data of Furuichi *et al.* (2015) agree well for the Re_b range studied. Fitting our DNS data with (3.1) yields $A = 2.039 \pm 0.083$, $B = 0.948 \pm 0.364$ with uncertainty estimates based on 95 % confidence bounds, giving $\kappa = 0.399 \pm 0.015$. The value reported by Pirozzoli *et al.* (2021) (i.e. $A = 2.102$, $B = 1.148$) are slightly larger than ours but still within the uncertainty range. However, large uncertainty is present in the fitted values due to the limited data points in Re. In addition, as Re_b is still relatively low, the reported value of $\kappa = 0.399 \pm 0.015$ should not be used outside of the given Re range. As will be shown in § 3.4, even for the highest Re_b case, a distinct logarithmic region does not manifest itself in the mean velocity profile $U(y)$. Higher Re data (e.g. $Re_\tau \geq 10^4$) are required to better estimate the constants in (3.1) and the associated κ values.

3.3. *Wall shear stress fluctuations*

The Re-dependence of axial wall shear stress fluctuation $\langle \tau_{z,w}'^2 \rangle^+$ is one of the highly debated issues in wall turbulence. Note that $\langle \tau_{z,w}'^2 \rangle^+$ is also equivalent to the wall dissipation of the axial Reynolds stress component $\epsilon_{z,w}^+$, the azimuthal vorticity variance at the wall $\langle \omega_\theta'^2 \rangle^+$ or the limiting value of $\langle u_z'^2 \rangle^+/U^2$ at the wall (Örlü & Schlatter 2011). Previous DNS studies of channel, pipe and turbulent boundary layer observed an increase in $\langle \tau_{z,w}'^2 \rangle^+$ with Re_τ, which reflects the increased contribution of large-scale motions to wall shear stress at high Re values (Marusic, Mathis & Hutchins 2010*a*). However, the exact dependence of $\langle \tau_{z,w}'^2 \rangle^+$ on Re_τ is not well established. For example, Örlü & Schlatter (2011) suggested that the r.m.s. $\langle \tau_{z,w}'^2 \rangle^+$ follows

$$\langle \tau_{z,w}'^2 \rangle^{+1/2} = C + D \ln(Re_\tau), \tag{3.2}$$

where the two constants C and D are chosen as 0.298 and 0.018 based on the DNS of turbulent boundary layer data.

Some works (Yang & Lozano-Durán 2017; Smits *et al.* 2021) also suggested that

$$\langle \tau_{z,w}'^2 \rangle^+ = E + F \ln(Re_\tau). \tag{3.3}$$

Re_τ	$10^2\lambda$	$\langle u_z'^2\rangle_p^+$	$-\langle u_r'u_z'\rangle_p^+$	$\langle \tau_{z,w}'^2\rangle^+$	$\langle \tau_{\theta,w}'^2\rangle^+$	$p_{w,rms}^+$	$p_{p,rms}^+$
181	3.730 (0.20 %)	7.229 (0.41 %)	0.719 (0.34 %)	0.123 (0.54)	0.031 (1.18 %)	1.721 (1.10 %)	2.039 (0.90 %)
549	2.672 (0.10 %)	7.587 (0.14 %)	0.861 (0.13 %)	0.158 (0.14 %)	0.063 (0.34 %)	2.283 (0.62 %)	2.720 (0.69 %)
998	2.244 (0.14 %)	7.968 (0.23 %)	0.902 (0.13 %)	0.170 (0.14 %)	0.071 (0.15 %)	2.569 (0.50 %)	3.020 (0.38 %)
2001	1.859 (0.22 %)	8.522 (0.14 %)	0.932 (0.14 %)	0.184 (0.18 %)	0.079 (0.18 %)	2.793 (0.67 %)	3.273 (0.54 %)
5197	1.498 (0.24 %)	9.117 (0.21 %)	0.957 (0.12 %)	0.196 (0.16 %)	0.082 (0.28 %)	3.174 (0.80 %)	3.610 (0.70 %)

Table 3. Summary of values and standard deviations of some key parameters: the friction factor $\lambda = 8\tau_{z,w}/(\rho U_b^2)$; the peak of axial velocity variance $\langle u_z'^2\rangle_p^+$; the peak of the Reynolds shear stress $-\langle u_r'u_z'\rangle_p^+$; the axial $\langle \tau_{z,w}'^2\rangle^+$ and azimuthal $\langle \tau_{\theta,w}'^2\rangle^+$ wall shear stress fluctuations; and the wall $(p_{w,rms}^+)$ and peak $(p_{p,rms}^+)$ values of root-mean-square (r.m.s.) pressure fluctuations.
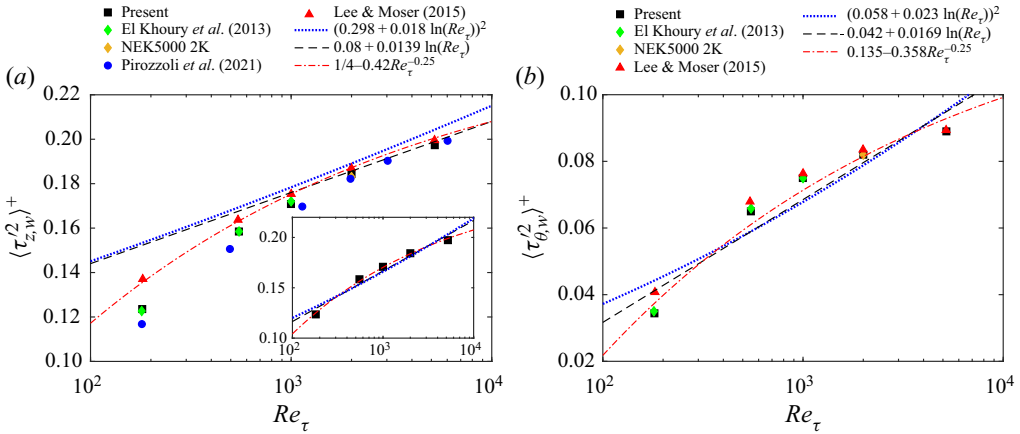
Figure 4. (*a*) Axial ($\langle \tau_{z,w}'^2 \rangle^+$) and (*b*) azimuthal ($\langle \tau_{\theta,w}'^2 \rangle^+$) wall shear stress fluctuations as a function of Re_τ. The dotted, dashed and dashed-dotted lines in the inset of (*a*) denote $\langle \tau_{z,w}'^2 \rangle^+ = (0.225 + 0.0264\ln(Re_\tau))^2$, $\langle \tau_{z,w}'^2 \rangle^+ = 0.016 + 0.0218\ln(Re_\tau)$ and $\langle \tau_{z,w}'^2 \rangle^+ = 0.255 - 0.477\,Re_\tau^{-1/4}$, respectively.

By fitting turbulent channel flow data of Lee & Moser (2015) and pipe flow data of Pirozzoli *et al.* (2021) for $Re_\tau \geq 1000$, Smits *et al.* (2021) obtained $E = 0.08$ and $F = 0.0139$.

Recently, Chen & Sreenivasan (2021) proposed a defect-power law, given as

$$\langle \tau_{z,w}'^2 \rangle^+ = \epsilon_{z,w}^+ = G - H\,Re_\tau^{-1/4}, \tag{3.4}$$

where G is the asymptotic value at infinite Re, and H is a coefficient. The assumption for (3.4) is that the dissipation of the axial Reynolds stress component ($\epsilon_z^+ = \nu\,\langle (\partial u_z^+/\partial x_j^+)(\partial u_z^+/\partial x_j^+) \rangle$) balances the turbulent kinetic energy production ($P_k = -\langle u_r u_z \rangle^+\,(\partial U^+/\partial y^+)$) near the location of peak production. The fact that P_k is bounded by $1/4$ (Sreenivasan 1989; Pope 2000) implies that $\epsilon_{z,w}^+$ may also stay bounded, which is further assumed by Chen & Sreenivasan (2021) to be the same bound of P_k, i.e. $G = 1/4$ (Chen & Sreenivasan 2021). This argument was later criticized by Smits *et al.* (2021) for the following two reasons. First, based on the DNS data, the location of peak production is actually the place where the largest imbalance of production and dissipation occurs. Second, as the balance between different terms in the Reynolds stress transport equation changes rapidly near the wall, it is unclear how the balance between P_k and $\epsilon_{z,w}^+$ can be extended up to the wall, where $P_k = 0$, and $\epsilon_{z,w}^+$ equals the viscous diffusion.

The axial wall shear stress fluctuation $\langle \tau_{z,w}'^2 \rangle^+$ as a function of Re_τ is depicted in figure 4(*a*). Akin to the observation in El Khoury *et al.* (2013), the values for the pipe are slightly lower than those for the channel, but the difference decreases with increasing Re_τ. Note that the data of Pirozzoli *et al.* (2021) are slightly lower than others, which is consistent with the lower λ in figure 3. The logarithmic law (3.2) proposed by Örlü & Schlatter (2011) is higher than the DNS data. This is somehow expected as the fitting coefficients were obtained based on the DNS of turbulent boundary layer data, which are higher than in pipe and channel. In the high Re_τ range, both the logarithmic (3.3) and defect-power-law scalings (3.4) agree well with the data. However, both scalings exhibit notable disagreements in the low Re_τ range. The discrepancy seems not particularly surprising, given that the parameters in these equations are obtained from different datasets and different Re_τ ranges. As a reference, the inset in figure 4(*a*) shows the fitting results
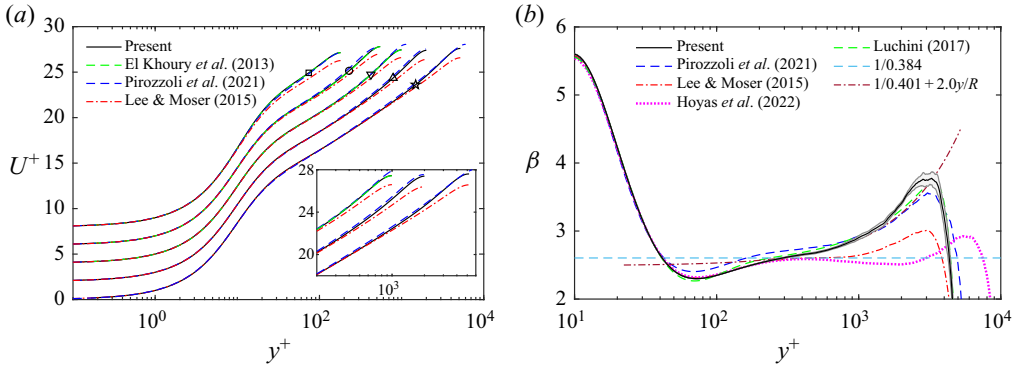
956 A18-11

Figure 5. (*a*) Mean velocity profiles U^+ and (*b*) log-law diagnostic function β. Profiles in (*a*) are offset vertically by two wall units, and the shaded area in (*b*) represents the standard deviation of our data at $Re_\tau = 5200$.

of (3.2)–(3.4) using our DNS data only. The fitted values are $C = 0.225$, $D = 0.0264$ for (3.2), $E = 0.016$, $F = 0.0218$ for (3.3), and $G = 0.255$, $H = 0.477$ for (3.4). For the Re_τ range studied, the data seem to match better the defect-power law but with a slightly higher asymptotic value than suggested by Chen & Sreenivasan (2021). Additional data at higher Re_τ are needed to confirm this finding.

Figure 4(*b*) further shows the azimuthal wall shear stress fluctuation $\langle \tau_{\theta,w}'^2 \rangle^+$ as a function of Re_τ. Similar to findings for $\langle \tau_{z,w}'^2 \rangle^+$, our data agree well with El Khoury *et al.* (2013) and NEK5000 2K cases, and all of them become closer to Lee & Moser (2015) with increasing Re_τ. Fitting data with the logarithmic and defect-power law yields $\langle \tau_{\theta,w}'^2 \rangle^+ = (0.058 + 0.023 \ln(Re_\tau))^2$, $\langle \tau_{\theta,w}'^2 \rangle^+ = -0.040 + 0.016 \ln(Re_\tau)$ and $\langle \tau_{\theta,w}'^2 \rangle^+ = 0.135 - 0.353 \, Re_\tau^{-1/4}$. Again, the defect-power law seems to match better the DNS data, but the agreement is not as good as for $\langle \tau_{z,w}'^2 \rangle^+$.

3.4. *Mean velocity profile*

In an overlap region between the inner and outer flows, there is a logarithmic variation of the mean axial velocity U^+ profile, which is given as

$$U^+ = \frac{1}{\kappa} \ln y^+ + B. \tag{3.5}$$

In a true log layer, the indicator function $\beta = y^+ (\partial U^+ / \partial y^+)$ is constant and equals $1/\kappa$.

The U^+ profiles at different Re_τ are compared to previous DNS data in figure 5(*a*). First, as expected, the wake in U^+ for the pipe is stronger than in the channel by Lee & Moser (2015). Second, our data in the outer region agree well with those of El Khoury *et al.* (2013), but not with Pirozzoli *et al.* (2021). This discrepancy was also noted by Pirozzoli *et al.* (2021), who found that their data, along with those of Wu & Moin (2008) and Ahn *et al.* (2013), differ from those of El Khoury *et al.* (2013) and Chin *et al.* (2014). This disparity is probably due to the numerical methods, where all of the former used low-order finite difference methods, while the latter two used high-order spectral-element methods.

The log-law diagnostics function β is shown in figure 5(*b*) for all high DNS data (i.e. $Re_\tau > 5000$). Interestingly, β for our $Re_\tau \approx 5200$ agrees with the channel data of Lee &

Moser (2015) and Hoyas *et al.* (2022) up to $y^+ \approx 250$. Note that a relatively small domain size was used by Hoyas *et al.* (2022), but it is assumed large enough to yield accurate flow statistics (Lozano-Durán & Jiménez 2014). This suggests a near-wall universality of the inner scaled mean velocity – similar to that observed by Monty *et al.* (2009). For all three cases, the trough is $\beta \approx 2.30$, located at $y^+ \approx 70$. However, the data of Pirozzoli *et al.* (2021) deviate from others for $y^+ > 40$ and have a larger magnitude of the trough, which is somewhat consistent with the slight upward shift of the U^+ observed in figure 5(*a*). This discrepancy is significantly larger than the statistical uncertainty (see Appendix B). Unlike channel flow, where a plateau starts to develop for $Re_\tau \geq 5200$, there is no plateau for pipe flow – suggesting that the minimum Re_τ for U^+ to develop a logarithmic region should be higher in the pipe than in the channel. The β in the wake region of the pipe is distinctly larger than the channel, implying a notable difference in flow structures in the core region between these two flows (Chin *et al.* 2014).

High-order corrections to the log-law relation (3.5) were sometimes introduced to better describe the mean velocity profile in the overlap region (Buschmann & Gad-el Hak 2003; Luchini 2017; Cantwell 2019). For example, based on refined overlap arguments expressed by Afzal & Yajnik (1973), Jiménez & Moser (2007) proposed the indicator function

$$\beta = \left(\frac{1}{\kappa_\infty} + \frac{\alpha_1}{Re_\tau} \right) + \alpha_2 \frac{y}{R}, \tag{3.6}$$

where α_1 and α_2 are adjustable constants, and κ_∞ is the asymptotic von Kármán constant. Equation (3.6) allows for a *Re*-dependence of $\kappa = \kappa_\infty + (\alpha_1/Re_\tau)^{-1}$ and introduces a linear dependence on *y*. By fitting our $Re_\tau \approx 5200$ data in the region between $y^+ = 300$ and $y = 0.16$, we obtain $\kappa = 0.401$ and $\alpha_2 = 2.0$. This κ is very close to 0.399 estimated from the friction factor relation (3.1) and 0.402 reported by Jiménez & Moser (2007) using channel data of $Re_\tau = 1000$ from Del Alamo *et al.* (2004), and $Re_\tau = 2000$ from Hoyas & Jiménez (2006). It is slightly larger than 0.387 by Pirozzoli *et al.* (2021) and 0.384 by Lee & Moser (2015). In addition, α_2 is generally much larger in the pipe than in the channel – suggesting a strong geometry effect on β. The value of $\alpha_2 = 2$ is consistent with the finding by Luchini (2017), who suggested that the logarithmic law of the velocity profile is universal across different geometries of wall turbulence, provided that the perturbative effect of the pressure gradient is taken into consideration. Furthermore, a good collapse between our data and the analytical prediction by Luchini (2017) is seen in figure 5(*b*).

3.5. *Reynolds stresses*

The non-zero components of the Reynolds stress tensor (or the velocity variances and covariance) are examined in this subsection (figures 6–10). For all datasets, the inner-scaled velocity variances and covariance increase with Re_τ in the whole wall-normal range. In terms of the axial velocity variance $\langle u_z'^2 \rangle^+$ (figure 6*a*), our data agree well with El Khoury *et al.* (2013) but differ from Pirozzoli *et al.* (2021), which is notably smaller in the near-wall region, particularly at low Re_τ. For the highest Re_τ cases, the agreement is reasonably good near the wall. However, note that the Pirozzoli *et al.* (2021) simulation is at a slightly higher Re_τ (i.e. ~ 6000). The differences between our case and that of Pirozzoli *et al.* (2021) can be better highlighted in the diagnostic plot (figure 6*b*), where the r.m.s. axial velocity fluctuation $u_{z,rms}'$ is plotted against the mean velocity U^+.
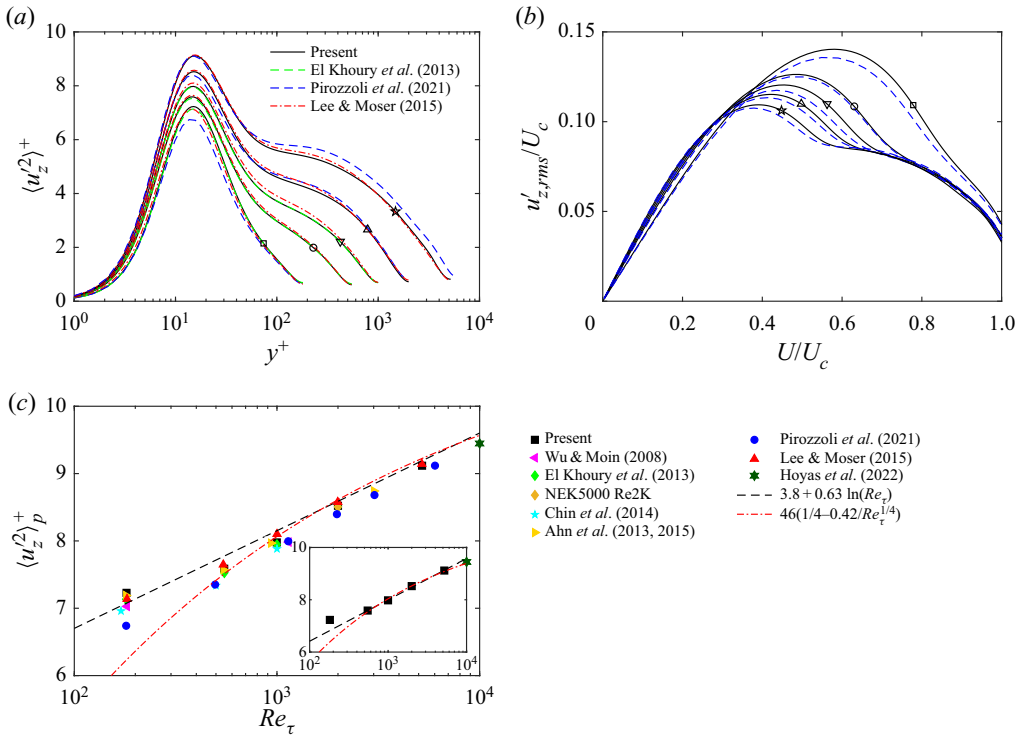
Figure 6. (*a*) Axial velocity variance $\langle u_z'^2 \rangle^+$ as a function of y^+; (*b*) the diagnostic plot depicting $u_{z,rms}'/U_c$ as a function of U^+/U_c; and (*c*) the inner peak of axial velocity variance $\langle u_z'^2 \rangle_p^+$ as a function of y^+. The dashed and dashed-dotted lines in the inset of (*c*) denote $\langle u_z'^2 \rangle_p^+ = 3.251 + 0.687 \ln(Re_\tau)$ and $\langle u_z'^2 \rangle_p^+ = 11.132 - 17.402 \, Re_\tau^{-1/4}$, respectively.

The diagnostic plot was introduced by Alfredsson & Örlü (2010) to assess if the mean velocity and velocity fluctuation profiles behave correctly without the need to determine the friction velocity or the wall position. Consistent with the observation in Alfredsson & Örlü (2010), the diagnostic plot collapses in the outer region for $Re_\tau > 180$, and has a clear Re trend around the peak value. Most importantly, the data by Pirozzoli *et al.* (2021) are consistently lower than ours, particularly in the near-wall region. Such inconsistency is also observed for $\langle u_\theta'^2 \rangle^+$ (figure 10). The agreement for $\langle u_r'^2 \rangle^+$ (figure 7*a*) is reasonably good among different pipe flow datasets, which is slightly larger than the channel, particularly in the outer region. The Reynolds shear stress $\langle u_r' u_z' \rangle^+$ shows excellent agreement among different datasets, even including the channel.

Let us focus now on the inner peak of the axial velocity variance $\langle u_z'^2 \rangle^+$. The inner peak is assumed to increase logarithmically with Re_τ – similar to the wall shear stress fluctuations due to the increased modulation effect of the large-scale structures in the logarithmic layer (Marusic & Monty 2019). Chen & Sreenivasan (2021) suggested recently that the growth of $\langle u_z'^2 \rangle^+$ would eventually saturate. The argument is based on the balance between the viscous diffusion and dissipation at the wall, and the Taylor series expansion of the axial velocity variance near the wall, given as

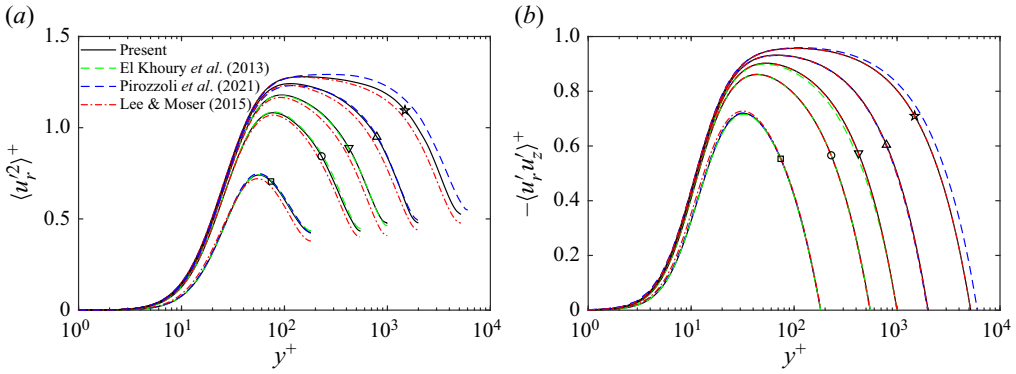$$\langle u_z'^2 \rangle^+ \sim D_{z,w}^+ y^{+2} = \epsilon_{z,w}^+ y^{+2}. \tag{3.7}$$

Figure 7. (*a*) Radial velocity variance $\langle u_r'^2 \rangle^+$, and (*b*) Reynolds shear stress $\langle u_r' u_z' \rangle^+$, as functions of y^+.
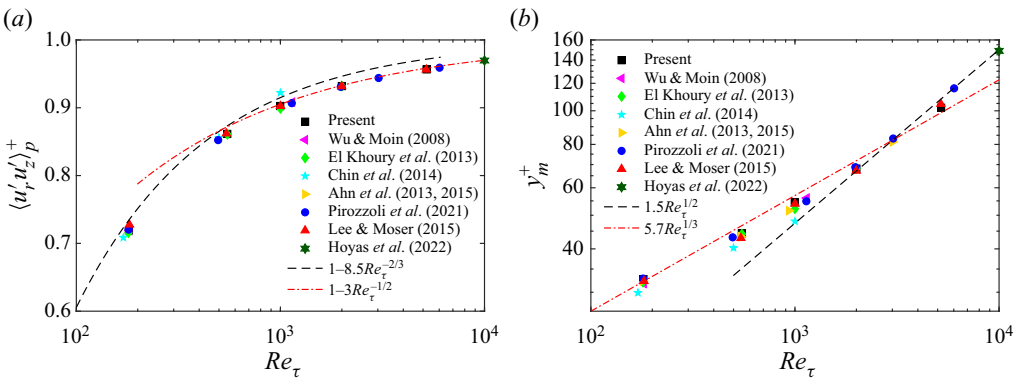

Figure 8. Reynolds number dependence of (*a*) the peak of the Reynolds shear stress $\langle u_r' u_z' \rangle^+$, and (*b*) the corresponding peak location in wall units.
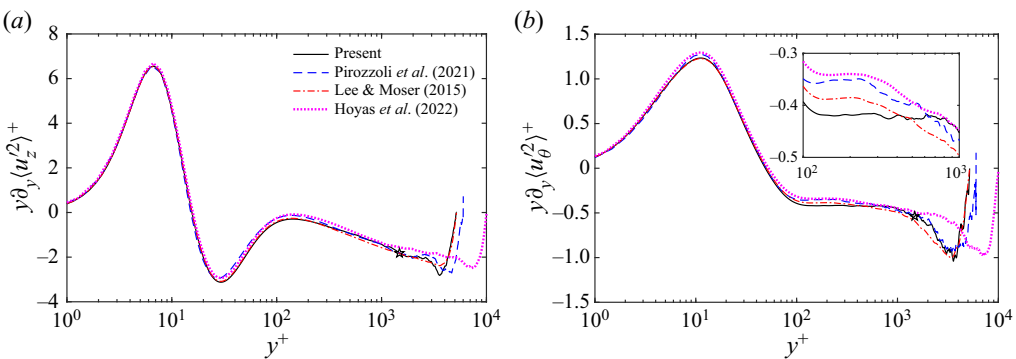

Figure 9. Indicator function for Townsend's prediction among different high-Re simulations: (*a*) axial velocity variance $y\,\partial_y \langle u_z'^2 \rangle^+$, and (*b*) azimuthal velocity variance $y\,\partial_y \langle u_\theta'^2 \rangle^+$.

Note that a similar expression is obtained in Smits *et al.* (2021), where the axial wall dissipation is used instead, i.e. $\langle u_z'^2 \rangle^+ \sim \langle \tau_{z,w}'^2 \rangle^+ y^{+2}$. If the assumption of the boundedness of wall dissipation (3.4) is valid and the inner peak location of $\langle u_z'^2 \rangle^+$ (denoted as $y_{z,p}^+$) is

956 A18-15
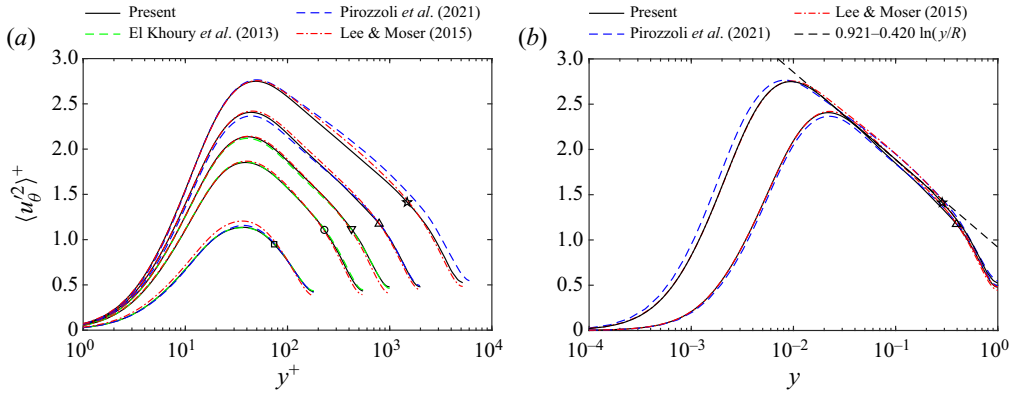
Figure 10. Azimuthal velocity variance $\langle u_\theta'^2 \rangle^+$ as a function of (a) y^+ and (b) y/R. Only the two highest Re_τ cases are included in (b).

independent of Re_τ, then (3.7) suggests that the peak of axial velocity variance should also be bounded in a defect-power form similar to the wall shear stress fluctuation:

$$\langle u_z'^2 \rangle_p^+ = M - N Re_\tau^{-1/4}, \tag{3.8}$$

where M is the asymptotic value and N is the coefficient.

This validity of (3.8) was challenged recently by Pirozzoli *et al.* (2021), who, based on their data, observed a slight increase of $y_{z,p}^+$ with Re_τ, from $y_{z,p}^+ = 14.28$ for $Re_\tau \approx 500$ to 15.14 for $Re_\tau \approx 6000$. We emphasize that such variation of $y_{z,p}^+$ with Re_τ is not observed in our case, where much finer near-wall resolutions than in Pirozzoli *et al.* (2021) are used. The value of $y_{z,p}^+$ is approximately 15 for all Re_τ (e.g. $y_{z,p}^+ = 15.07, 15.03, 15.50$ for $Re_\tau = 180, 2000, 5000$, respectively) – akin to the findings by many others (Moser *et al.* 1999; Jiménez *et al.* 2010; Chin *et al.* 2014; Smits *et al.* 2021).

Figure 6(c) shows $\langle u_z'^2 \rangle_p^+$ for all the DNS data listed in table 2, along with the logarithmic law $\langle u_z'^2 \rangle_p^+ = 3.8 + 0.64 \ln(Re_\tau)$ by Marusic *et al.* (2017) and the power law $\langle u_z'^2 \rangle_p^+ = 11.5 - 19.32 Re_\tau^{-1/4}$ by Chen & Sreenivasan (2021). The difference between different DNS datasets is relatively small, except for those from Pirozzoli *et al.* (2021), which are consistently lower than others for all Re_τ. Note that this discrepancy is much larger than the uncertainty (standard deviation), which is less than 0.5 % (see table 3). Both the logarithmic and defect-power laws fit well with the data in the high Re_τ range but have certain discrepancies at low Re_τ. This suggests that there might exist a transitional scaling – similar to that found for the Reynolds shear stress (Chen, Hussain & She 2019). The parameters in these two scaling laws can be adjusted to better fit our dataset. The inset shows the fitting results for our data without the one at $Re_\tau = 180$: $\langle u_z'^2 \rangle_p^+ = 3.251 + 0.687 \ln(Re_\tau)$ and $\langle u_z'^2 \rangle_p^+ = 11.132 - 17.402 Re_\tau^{-1/4}$. With these new constants, the agreement is improved for both scaling laws. In summary, for the Re_τ range studied, both scaling laws provide a good match with $\langle u_z'^2 \rangle_p^+$ data when the fitting parameters are properly adjusted. Data at even higher Re_τ are required to determine which law is more consistent with the data.

According to Townsend's attached eddy hypothesis, at sufficiently high *Re*, the Reynolds stress components in a certain *y* range satisfy

$$\langle u_z'^2 \rangle^+ = A_1 - B_1 \ln(y/R), \tag{3.9}$$

$$\langle u_z'^2 \rangle^+ = A_2, \tag{3.10}$$

$$\langle u_\theta'^2 \rangle^+ = A_3 - B_3 \ln(y/R), \tag{3.11}$$

$$\langle u_r' u_z' \rangle^+ = -1, \tag{3.12}$$

where A_i and B_i are universal constants.

Consistent with these relations, the radial velocity variance $\langle u_r'^2 \rangle^+$ slowly develops a flat region as Re_τ increases. In addition, the Reynolds shear stress $\langle -u_r' u_z' \rangle^+$ profiles also tend to become flattened at higher Re_τ. As noted by Afzal (1982), the peak Reynolds shear stress at high Re_τ follows $\langle -u_r' u_z' \rangle_p^+ \approx 1 - 2/\sqrt{\kappa\, Re_\tau}$, and the corresponding position y_m^+ shifts away from the wall following $y_m^+ \sim \sqrt{Re_\tau/\kappa}$. Chen *et al.* (2019) suggested that there is a non-universal scaling transition, where the peaks at low Re_τ scales as $\langle u_r' u_z' \rangle_p^+ \approx Re_\tau^{-2/3}$ and their locations scales as $y_m^+ \sim Re_\tau^{1/3}$. Figure 8 shows $\langle -u_r' u_z' \rangle_p^+$ and the corresponding y_m^+ as a function of Re_τ. For $Re_\tau > 1000$, $Re^{-1/2}$ for $\langle -u_r' u_z' \rangle_p^+$ and $Re^{-1/2}$ for y_m^+ are satisfied with good accuracy, and at the low Re_τ range, $Re_\tau^{-2/3}$ for $\langle -u_r' u_z' \rangle_p^+$ and $Re_\tau^{-1/3}$ for y_m^+ scalings proposed by Chen *et al.* (2019) also yield good agreement.

Regarding the axial velocity variance $\langle u_z'^2 \rangle^+$, the indicator function is not flat anywhere in the domain (figure 9*a*) – suggesting that no clear logarithmic region develops for the Re_τ range considered. As discussed in Lee & Moser (2015), $Re_\tau = 5200$ is not quite high enough to exhibit such a region. Based on the Superpipe data, Marusic *et al.* (2013) suggested that a sensible logarithmic layer emerges only for $Re_\tau > 10^4$. Consistent with the findings in Lee & Moser (2015) and Pirozzoli *et al.* (2021), the azimuthal velocity variance $\langle u_\theta'^2 \rangle^+$ develops the logarithmic layer at lower Re_τ. The indicator function of $\langle u_\theta'^2 \rangle^+$ shows a distinct plateau (figure 9*b*). Interestingly, when compared with other cases, the range of the logarithmic layer is wider in our $Re_\tau \approx 5200$ case. Fitting the data in the range $120 \leq y^+ \leq 800$ yields $A_3 = 0.921$, $B_3 = 0.420$, which are close to $A_3 = 1.0$, $B_3 = 0.40$ by Pirozzoli *et al.* (2021), and between $A_3 = 1.08$, $B_3 = 0.387$ obtained by Lee & Moser (2015) for the turbulent channel and $A_3 = 0.8$, $B_3 = -0.45$ by Sillero, Jiménez & Moser (2013) in the turbulent boundary layer.

3.6. *Production and dissipation of the turbulent kinetic energy*

Figure 11(*a*) shows the production P_k^+ and dissipation ϵ_k^+ $(= \nu\, \langle (\partial u_i'^+/\partial x_j^+)(\partial u_i'^+/\partial x_j^+) \rangle)$ of the turbulent kinetic energy (i.e. $k^+ = (\langle u_r'^2 \rangle^+ + \langle u_\theta'^2 \rangle^+ + \langle u_z'^2 \rangle^+)/2$). Other terms in the transport equations of the turbulent kinetic energy and individual Reynolds stress components are available at https://dataverse.tdl.org/dataverse/turbpipe. The production P_k^+ has a peak at around $y^+ \approx 11$, and the magnitude approaches the asymptotic value $1/4$ as Re_τ increases. Despite notable differences in the mean axial/streamwise velocity profile observed in the outer region, P_k^+ is quite similar between pipes and channels. This explains why the higher velocity gradient of the pipe does not contribute an effect to the turbulence intensities. The magnitude of dissipation ϵ_k^+ increases continuously with Re_τ,
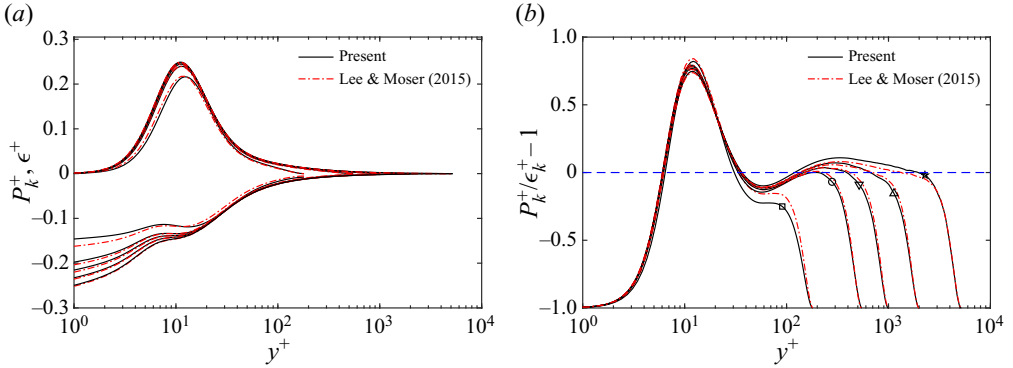
Figure 11. (a) Production P_k^+ and dissipation ϵ_k^+ of the turbulent kinetic energy, and (b) balance of production and dissipation $P_k^+/\epsilon_k^+ - 1$, as functions of y^+.

and the difference between the pipe and channel is mainly in the near-wall region and decreases with increasing Re_τ.

At sufficiently high Re_τ, there is an intermediate region where production balances dissipation. Recent numerical results (Lee & Moser 2015; Pirozzoli *et al.* 2021) suggest that such equilibrium between production and dissipation is violated due to the presence of LSMs and VLSMs. Figure 11(b) shows the relative excess of production over dissipation $(P_k^+/\epsilon_k^+ - 1)$. First, there is a near-wall region ($8 \le y^+ \le 35$) where P_k^+ distinctly exceeds ϵ_k^+. At high Re_τ, another region of $P_k^+/\epsilon_k^+ > 1$ develops, and the magnitude increases with Re_τ. For the $Re_\tau \approx 5200$ case, the peak imbalance is approximately 11 % (located at $y^+ \approx 330$), which is slightly larger than in the channel (i.e. 8 %).

3.7. *Mean pressure and r.m.s. pressure fluctuation*

The mean pressure and r.m.s. pressure fluctuations are displayed in figure 12. First, the mean pressure P^+ has different behaviour in the outer region between pipe and channel flows, with P^+ being substantially lower in the wake of the pipe. As discussed in El Khoury *et al.* (2013), this difference is related to the mean radial momentum equation, which, in pipe flow, is given as (Hinze 1975)

$$\frac{1}{\rho}\frac{\partial P}{\partial r} + \frac{\mathrm{d}}{\mathrm{d}r}\langle u_r'^2 \rangle + \frac{\langle u_r'^2 \rangle - \langle u_\theta'^2 \rangle}{r} = 0. \tag{3.13}$$

By changing variable (i.e. $r = R - y$) and then integrating the above equation, the mean pressure for pipe flow with the wall value set to zero can be expressed as

$$P^+(y) = -\langle u_r'^2 \rangle^+ + \int_0^y \frac{\langle u_r'^2 \rangle^+ - \langle u_\theta'^2 \rangle^+}{R - y'}\,\mathrm{d}y'. \tag{3.14}$$

In channel flow, the last term on the left-hand side of (3.13) is absent, and the mean pressure is solely balanced by the wall-normal velocity fluctuation, i.e. $P^+(y) = -\langle v'^2 \rangle^+$. From figure 7(a), it is clear that the wall-normal velocity fluctuation is comparable between pipe and channel flows. However, as $\langle u_r'^2 \rangle^+ < \langle u_\theta'^2 \rangle^+$ in pipe flow, the extra term in (3.14) is zero at the wall and decreases with increasing y – resulting in a lower pressure in pipes than in channels.
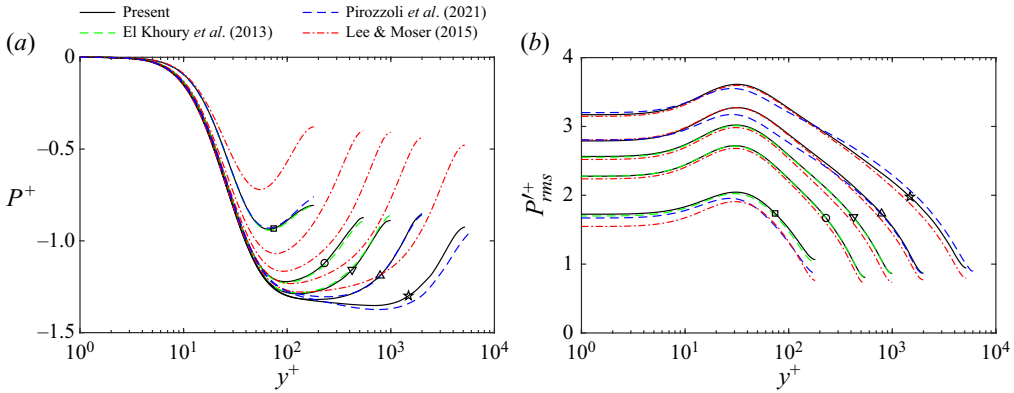
956 A18-18

Figure 12. (*a*) Mean pressure (P^+) and (*b*) r.m.s. pressure fluctuation (P'^+_{rms}), as functions of y^+.
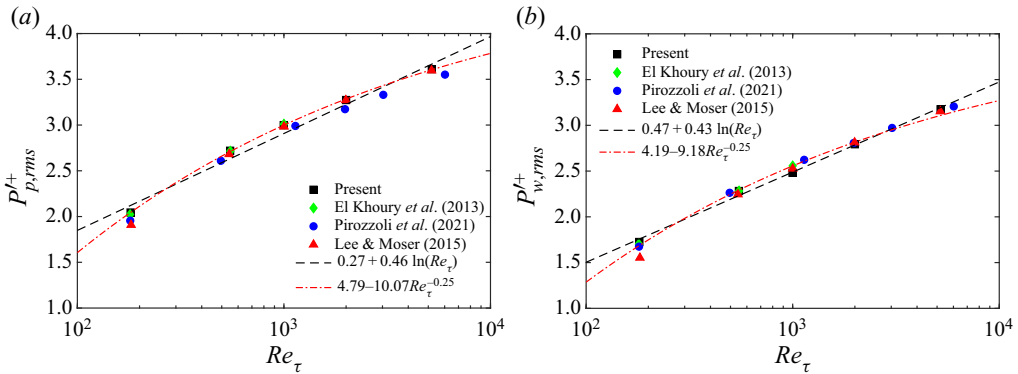

Figure 13. Reynolds number dependence of (*a*) peak ($P'^+_{p,rms}$) and (*b*) wall ($P'^+_{w,rms}$) values of r.m.s. pressure fluctuations.

Similar to that observed by El Khoury *et al.* (2013), the r.m.s. pressure fluctuation p'^+_{rms} exhibits similar behaviour between the pipe and channel, except for slightly lower values for the latter. Minor differences are observed between our data and those of Pirozzoli *et al.* (2021), particularly near the peak value. The difference between our data and the channel data of Lee & Moser (2015) in the near-wall region decreases with increasing Re_τ. Figure 13 further shows the peak and wall values of p'^+_{rms}, which has similar Re-dependence as for other measures, such as wall shear stress fluctuations and axial velocity variances. Again, for the Re_τ studied, both the logarithmic and defect-power laws fit the data well.

3.8. *Energy spectra*

As Re increases, the separation of scales between the near-wall and outer-layer structures enlarges. In this section, the scale-separation is examined with one-dimensional velocity spectra for $Re_\tau \approx 5200$ (figure 14). The energy spectrum of axial velocity u_z in the axial direction has two distinct peaks – the inner one located at $k_z R = 40$ ($\lambda_z^+ = 816$) and $y^+ = 13$, and the outer one at $k_z R = 1$ ($\lambda_z = 2\pi R$), $y^+ = 400$. The dual-peak nature is more discernible in the azimuthal spectra with peaks at $k_\theta = 250$ ($\lambda_\theta^+ = 2\pi r^+/k_\theta = 131$), $y^+ = 13$ and $k_\theta = 6$ ($\lambda_\theta = 2\pi r/k_\theta = 0.846R$), $y^+ = 1000$. The k_θ values of all these
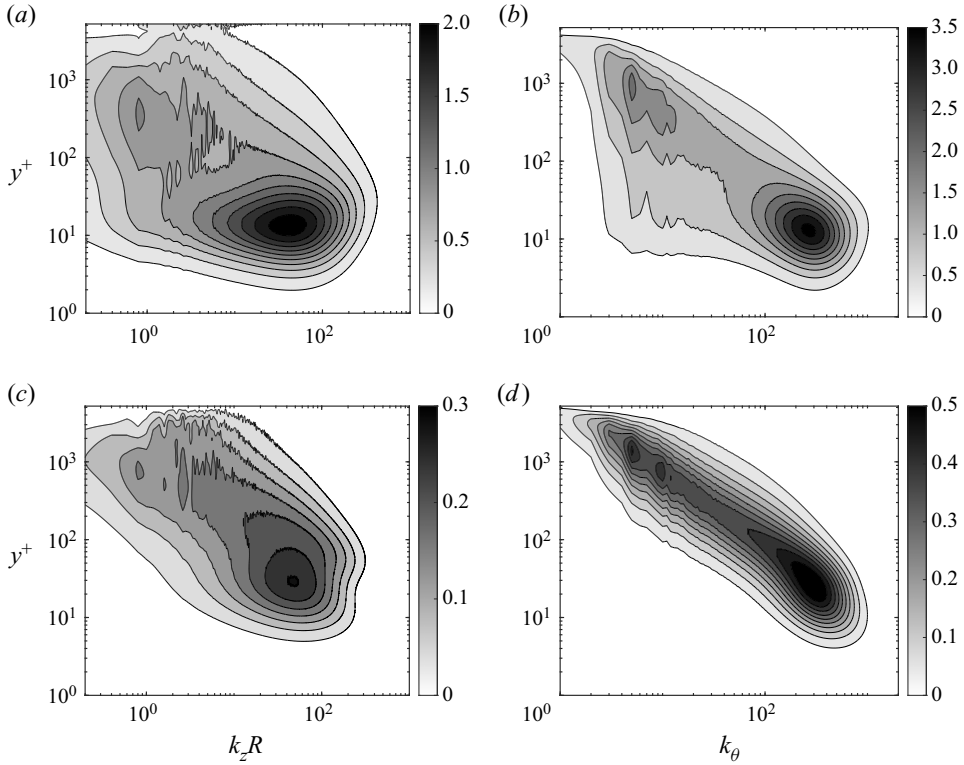
956 A18-19

Figure 14. Wavenumber pre-multiplied energy spectra for $Re_\tau = 5200$: (a) $k_z E_{zz}/u_\tau^2$, (b) $k_\theta E_{zz}/u_\tau^2$, (c) $k_z E_{rz}/u_\tau^2$, and (d) $k_\theta E_{rz}/u_\tau^2$.

peaks coincide with those found by Lee & Moser (2015) in the channel at the same Re_τ, but the physical scales are smaller than in the channel. It is well known that the inner peak at $y^+ = 13$ is associated with the streaks that are generated through the near-wall self-sustaining cycle (Waleffe 1997; Schoppa & Hussain 2002). As seen frequently in experiments (Hutchins & Marusic 2007; Monty *et al.* 2009; Rosenberg *et al.* 2013), the outer peak results from VLSMs. The outer peak in the θ-direction (at $y = 0.192$) is located farther away than the streamwise one (at $y = 0.077$), which according to Wu, Baltzer & Adrian (2012) suggests that the VLSMs in the outer region maintain their energy in the θ-direction more strongly than in the z-direction. The pre-multiplied energy spectra of the Reynolds shear stress in axial ($k_z E_{rz}/u_\tau^2$) and azimuthal ($k_\theta E_{rz}/u_\tau^2$) directions as functions of y^+ are shown in figures 14(c,d), respectively. The inner peak is located at $y^+ = 30$ with $k_z R = 49.2$ ($\lambda_\theta^+ = 664$) for $k_z E_{rz}/u_\tau^2$, and $k_\theta = 268$ ($\lambda_\theta^+ = 120$) for $k_\theta E_{rz}/u_\tau^2$. Compared with the axial velocity spectra, although the wavelength of the outer peak remains identical, the magnitude is much weaker and farther away from the wall.

Figure 15(a) shows the one-dimensional pre-multiplied energy spectra $k_z E_{zz}/u_\tau^2$ at different y locations. For comparison, the channel data of Lee & Moser (2015) at the same Re_τ are also included. First, good agreement is observed at $y^+ = 15$ between channel and pipe, particularly at higher wavenumbers – suggesting insignificance of pipe curvature on fine-scale near-wall structures. The scaling analysis of Perry, Henbest & Chong (1986) suggests that the energy spectral density of the axial velocity fluctuations $k_z E_{zz}/u_\tau^2$ should
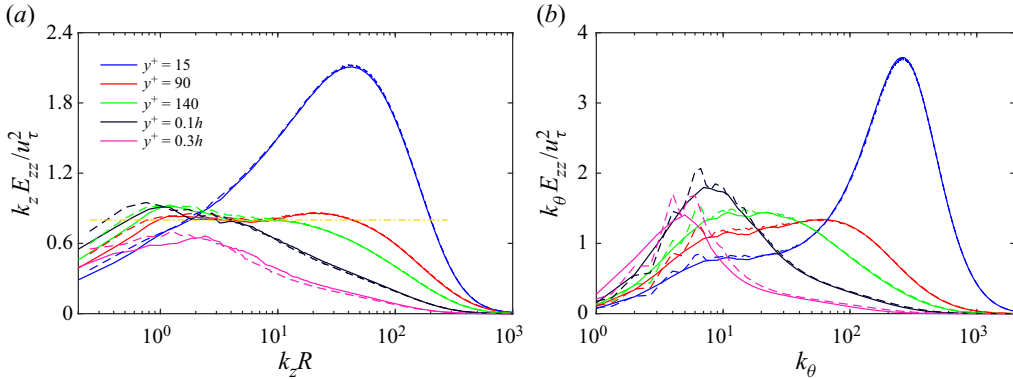
956 A18-20

Figure 15. Comparison of the pre-multiplied energy spectra between pipe (solid) and channel (dashed) for $Re_\tau = 5200$: (a) $k_z E_{zz}/u_\tau^2$, and (b) $k_\theta E_{zz}/u_\tau^2$.

vary as k_z^{-1} in the overlap region. The k_z^{-1} region has previously been observed in the high-Re experiments (Nickels *et al.* 2005; Rosenberg *et al.* 2013). Recently, such k_z^{-1} has also been discovered in DNS of turbulent channel flow at $Re_\tau = 5200$ (Lee & Moser 2015). Similarly, a plateau in the region $6 \leq k_z R \leq 10$ is observed for $90 \leq y^+ \leq 170$, and the magnitude 0.8 agrees with experiments (Nickels *et al.* 2005; Rosenberg *et al.* 2013). A bimodal is observed for $y^+ = 90$, with the peak magnitude at low wavenumbers ($k_z R = 1$) being smaller than at high wavenumbers ($k_z R = 30$). Interestingly, $k_z E_{zz}/u_\tau^2$ values at low wavenumbers are slightly smaller in the pipe than in the channel. Figure 15(b) further shows the one-dimensional pre-multiplied energy spectra $k_\theta E_{zz}/u_\tau^2$ at different y locations. Again, $k_\theta E_{zz}/u_\tau^2$ agrees well between the pipe and the channel at high wavenumbers. Consistent with those in the channel, a plateau appears for $5 \leq k_\theta \leq 30$ in the overlap region, with the magnitude increasing with y^+. Such a plateau is present even in the viscous sublayer, which is the footprint of LSMs and VLSMs near the wall (Mathis, Hutchins & Marusic 2009; Hwang *et al.* 2016).

4. Concluding remarks

A new direct numerical simulation providing reliable high-fidelity data of turbulent pipe flow for Re_τ up to 5200 is presented. Particular focus has been put on providing data that are as accurate as possible, by using a high-order numerical method, large domains and sufficient integration time with quantified uncertainty. The DNS are performed with a pseudo-spectral code OPENPIPEFLOW, and the axial extent of the domain is $10\pi R$ (where R is the pipe radius), which can be considered sufficiently long to capture all the relevant structures. A wealth of statistical data with uncertainty, including mean velocity, Reynolds stress and their budgets, pressure and its fluctuations, and energy spectra, are gathered (available online at https://dataverse.tdl.org/dataverse/turbpipe). An extensive comparison between our new pipe data and other simulation and experimental data is made, and small but still substantial and systematic differences between the various datasets are identified. For example, consistent lower values of the friction factor, wall shear stress fluctuations, and the inner peak of the axial velocity variance are observed for data generated using low-order methods, such as Ahn *et al.* (2013) and Pirozzoli *et al.* (2021). In pipe flow simulation, the only parameter apart from Re is the length of the pipe. Once the latter is chosen large enough, all data should, in principle, be the same.

Such discrepancies between different simulations thus highlight the need for high-order accurate methods for this particular flow case. This argument is further complemented by performing additional DNS at $Re_\tau = 2000$ with a spectral-element code NEK5000, where all the statistical data generated are found to match well the results obtained using OPENPIPEFLOW.

Different from turbulent channel flow, the mean velocity has not yet developed a logarithmic region at $Re_\tau = 5200$, yet the diagnostic function collapses well between our $Re_\tau \approx 5200$ and the channel data of Lee & Moser (2015) and Hoyas *et al.* (2022) up to $y^+ \approx 250$ – suggesting a near-wall universality of the inner scaled mean velocity. The wall shear stress fluctuations, the inner peak of axial velocity variance, and the wall and peak of r.m.s. pressure fluctuations continuously increase with Re_τ, and their difference between pipe and channel decreases with increasing Re_τ. In addition, at the Re_τ range considered, the Re dependence of these quantities agrees with both the logarithmic and defect-power scaling laws (Chen & Sreenivasan 2021). Consistent with observations in the channel, the one-dimensional spectrum of the axial velocity exhibits a k^{-1} dependence at intermediate distances from the wall.

Author ORCIDs.
- Jie Yao https://orcid.org/0000-0001-6069-6570;
- Saleh Rezaeiravesh https://orcid.org/0000-0002-9610-9910;
- Philipp Schlatter https://orcid.org/0000-0001-9627-5903;
- Fazle Hussain https://orcid.org/0000-0002-2209-9270.

Appendix A. Additional information regarding the DNS at $Re_\tau = 5200$

A comparison of the radial resolution Δy^+ between various high-Re DNS data is shown in figure 16. The corresponding Kolmogorov scale $\eta^+ = \epsilon_k^{+-1/4}$ is also included as a reference. Near the wall, Δy^+ for our simulation is smallest among all cases, and much smaller than η^+. For our case, Δy^+ increases progressively with y^+ and then reaches the maximum at $r/R \approx 0.44$. For the whole radial direction, Δy^+ is smaller than that of Lee & Moser (2015). In addition, it is less than $1.5\eta^+$, which, following standard practices, indicates that a sufficient amount of grid points are used.

The simulation was performed using 32 768 processors (Intel Xeon Platinum 8280) on the Frontera supercomputer at Texas Advanced Computing Center, and 16 384 processors
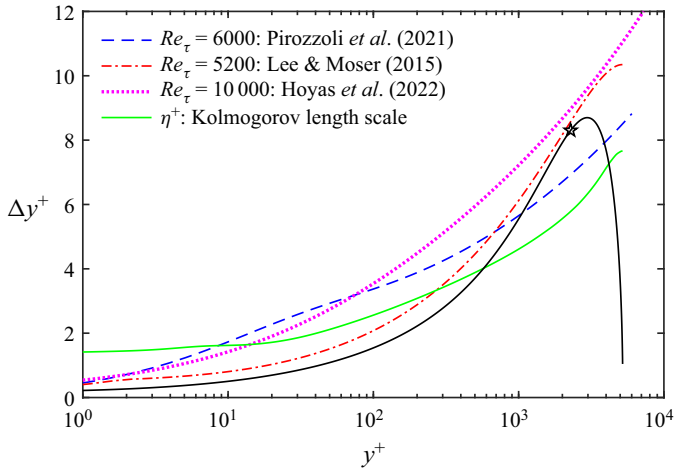
Figure 16. Comparison of the grid resolution in radial direction Δr^+ among different high-Re simulations. The black solid line with a star denotes our $Re_\tau \approx 5200$ result.

(AMD EPYC 7702) on Nocona at Texas Tech University High Performance Computing Center. A total of approximately 40π simulation time in terms of convective time units (R/U_b) after the transient period was collected for statistical averaging, which corresponds to approximately 500 000 steps with time step $\Delta t = 2.5 \times 10^{-4} R/U_b$.

Appendix B. Estimated uncertainties for one-point statistics

We explain briefly the approach employed to estimate the uncertainties in the mean velocity and Reynolds stress components of the DNS of the pipe flow. During the simulations, the time samples of the quantities contributing to statistical terms are averaged over the azimuthal (θ) and axial (z) directions. To compute the central statistical moments, the temporal correlations between the spatially averaged quantities are preserved by, for instance, writing a Reynolds stress component as $\langle u'_r u'_z \rangle = \langle \overline{u_r u_z} - \bar{u}_r \bar{u}_z \rangle$, where overbar means averaging over θ and z. In practice, the sample-mean estimator (SME) is used to estimate $\langle a \rangle$ from a finite number of time series samples $\{a_i\}_{i=1}^n$, where $a_i = a(t_i)$ are equispaced time samples. The SME for $\langle a \rangle$ is defined as

$$\hat{\mu}_a := \hat{\mathbb{E}}[a] = \frac{1}{n} \sum_{i=1}^n a_i, \tag{B1}$$

where $\hat{\mathbb{E}}[a]$ is the estimated expectation of a. Based on the central limit theorem, for a sufficiently large number of samples, the SME converges to the true expectation via a Gaussian distribution,

$$\hat{\mu}_a \sim \mathcal{N}(\mu_a, \sigma^2(\hat{\mu}_a)). \tag{B2}$$

To estimate $\sigma(\hat{\mu}_a)$ and hence quantify the time-averaging uncertainty in $\hat{\mu}_a$, an analytical expression can be derived that depends on the autocorrelation of time series a at different lags; see e.g. Oliver *et al.* (2014) and Rezaeiravesh *et al.* (2022). To avoid inaccuracy in $\sigma(\hat{\mu}_a)$ due to the oscillations in the sample-estimated autocorrelations,

956 A18-23

Re_τ	181	549	990	2001	5197
Sampling interval (R/U_b)	0.5	0.5	0.5	0.25	0.25
Number of samples	6228	1652	1301	1622	683

Table 4. Summary of the sampling of the flow variables used in the UQ analyses.

especially at higher lags, an autoregressive model is first fitted to the samples $\{a_i\}_{i=1}^n$, which is then used to construct a smooth model for the autocorrelations. The details of the approach can be found in Oliver *et al.* (2014) and D. Xavier *et al.* (personal communication 2022). The main hyperparameters of this uncertainty quantification (UQ) approach are the order of the autoregressive model and the number of training lags when modelling the autocorrelation function (ACF). In the present study, the optimal values of these hyperparameters are chosen based on the sampling frequency of the data at each *Re*. All estimations of uncertainties have been performed using UQit (Rezaeiravesh, Vinuesa & Schlatter 2021).

Following the above approach, the uncertainty in the statistical moments of any order can be estimated accurately. However, there are various turbulence statistics that are defined as a combination of the exponents of various moments; for instance, consider the turbulence intensity, r.m.s. fluctuations, turbulent kinetic energy, and various terms in the transport equations of the Reynolds stress components. The uncertainty in such terms can be estimated by applying the approach described in Rezaeiravesh *et al.* (2022). The main idea for estimating the uncertainty in a compound statistical term is to estimate the uncertainty in its constitutive statistical moments and also estimate the cross-covariance between the SMEs corresponding to them. Following this procedure, in the DNS database reported online in connection with the present study, all statistics are accompanied by an accurate estimation of the corresponding time-averaging uncertainty. An important aspect of this procedure is that for the statistics expressed in wall units, the uncertainty of the wall friction velocity is also taken into account. This means, for instance, that for $\langle u_r' u_z' \rangle^+$, the uncertainty of both $\langle u_r' u_z' \rangle$ and $\langle u_\tau \rangle^2$ are considered applying a Monte-Carlo-based UQ forward problem, which does not require any linearization.

Table 4 summarizes the sampling interval and the total number of samples used for UQ for simulations at different Re_τ. Our investigation showed that for the collected samples, an autoregressive model of order 20 along with the sample-estimated ACF at the first 20 lags, for $Re_\tau = 180$, 550 and 1000, and 40 lags, for $Re_\tau = 2000$ and 5200, leads to accurate models for autocorrelation of various quantities. For low-order moments, using sample-estimated ACF at a higher number of lags, especially near the centre of the pipe, could lead to slightly more accurate models for ACF. However, the difference in the resulting estimated uncertainty is below 1 %.

Figure 17 shows the standard deviation σ (see (B2)) of the sample estimation of different inner-scaled statistical terms. Clearly, the estimated uncertainties vary between the moments and also in the wall-normal direction. However, for all quantities, the lowest uncertainty (corresponding to highest certainty) is observed near the wall. Moreover, the estimated uncertainty for each quantity exhibits a similar variation in the wall-normal direction for different Re_τ.
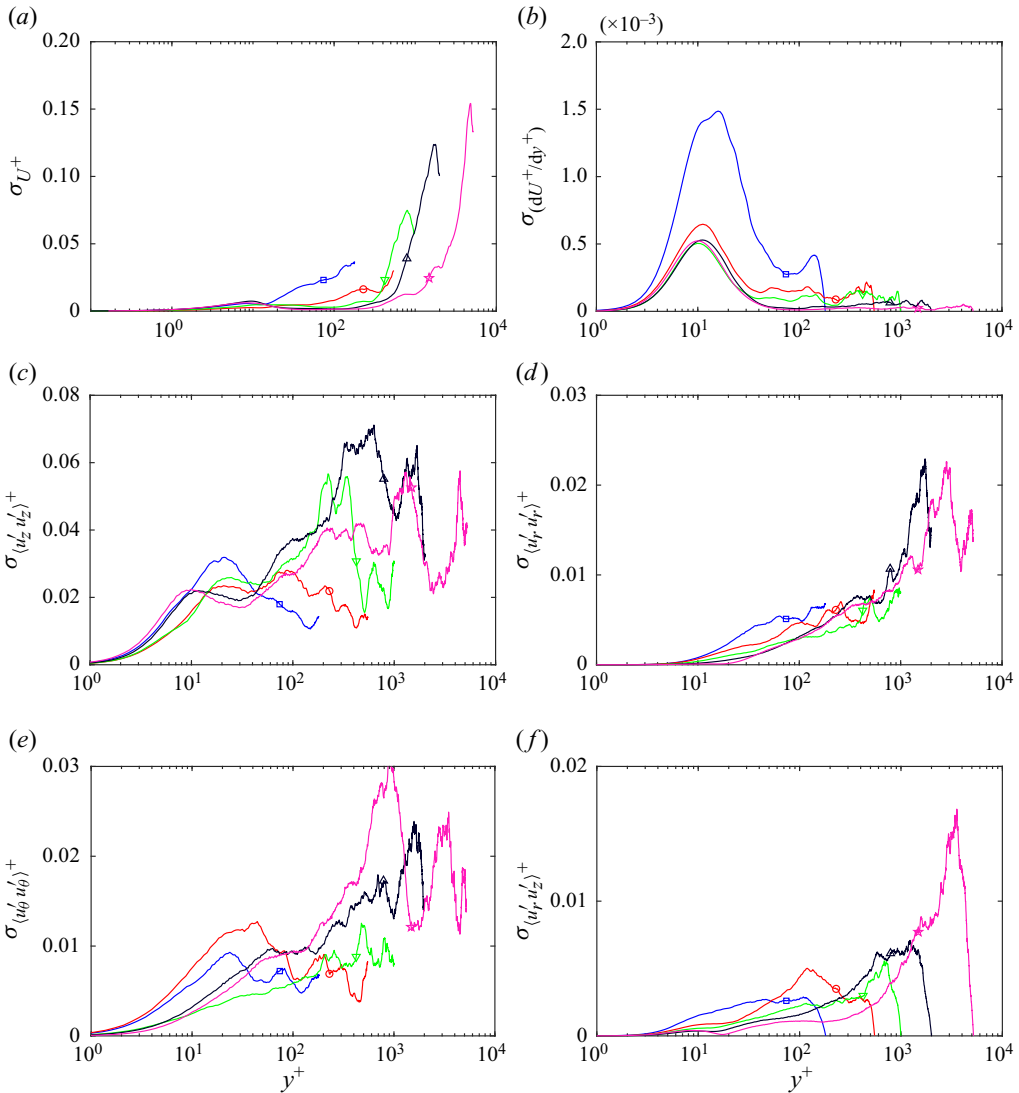
Figure 17. Estimated standard deviation of different statistical quantities: (*a*) U^+, (*b*) $\partial U^+/\partial y^+$, (*c*) $\langle u_z'^2 \rangle^+$, (*d*) $\langle u_r'^2 \rangle^+$, (*e*) $\langle u_\theta'^2 \rangle^+$, (*f*) $\langle u_r' u_z' \rangle^+$.

REFERENCES

AFZAL, N. 1976 Millikan's argument at moderately large Reynolds number. *Phys. Fluids* **19** (4), 600–602.

AFZAL, N. 1982 Fully developed turbulent flow in a pipe: an intermediate layer. *Ing.-Arch.* **52** (6), 355–377.

AFZAL, N. & YAJNIK, K. 1973 Analysis of turbulent pipe and channel flows at moderately large Reynolds number. *J. Fluid Mech.* **61** (1), 23–31.

AHN, J., LEE, J.H., JANG, S.J. & SUNG, H.J. 2013 Direct numerical simulations of fully developed turbulent pipe flows for $Re_\tau = 180$, 544 and 934. *Intl J. Heat Fluid Flow* **44**, 222–228.

AHN, J., LEE, J.H., LEE, J., KANG, J.-H. & SUNG, H.J. 2015 Direct numerical simulation of a 30*R* long turbulent pipe flow at $Re_\tau = 3008$. *Phys. Fluids* **27** (6), 065110.

ALFREDSSON, P.H. & ÖRLÜ, R. 2010 The diagnostic plot – a litmus test for wall bounded turbulence data. *Eur. J. Mech. B/Fluids* **29** (6), 403–406.

BERNARDINI, M., PIROZZOLI, S. & ORLANDI, P. 2014 Velocity statistics in turbulent channel flow up to $Re_\tau = 4000$. *J. Fluid Mech.* **742**, 171–191.

BLASIUS, H. 1913 Das Äehnlichkeitsgesetz bei Reibungsvorgängen in Flüssigkeiten. In *Mitteilungen über Forschungsarbeiten auf dem Gebiete des Ingenieurwesens*, pp. 1–41. Springer.

BUSCHMANN, M.H. & GAD-EL HAK, M. 2003 Generalized logarithmic law and its consequences. *AIAA J.* **41** (1), 40–48.

CANTON, J., ÖRLÜ, R., CHIN, C., HUTCHINS, N., MONTY, J. & SCHLATTER, P. 2016 On large-scale friction control in turbulent wall flow in low Reynolds number channels. *Flow Turbul. Combust.* **97** (3), 811–827.

CANTWELL, B.J. 2019 A universal velocity profile for smooth wall pipe flow. *J. Fluid Mech.* **878**, 834–874.

CHEN, X., HUSSAIN, F. & SHE, Z.-S. 2019 Non-universal scaling transition of momentum cascade in wall turbulence. *J. Fluid Mech.* **871**, R2.

CHEN, X. & SREENIVASAN, K.R. 2021 Reynolds number scaling of the peak turbulence intensity in wall flows. *J. Fluid Mech.* **908**, R3.

CHIN, C., MONTY, J.P. & OOI, A. 2014 Reynolds number effects in DNS of pipe flow and comparison with channels and boundary layers. *Intl J. Heat Fluid Flow* **45**, 33–40.

DEL ALAMO, J.C., JIMÉNEZ, J., ZANDONADE, P. & MOSER, R.D. 2004 Scaling of the energy spectra of turbulent channels. *J. Fluid Mech.* **500**, 135–144.

DOGAN, E., ÖRLÜ, R., GATTI, D., VINUESA, R. & SCHLATTER, P. 2018 Quantification of amplitude modulation in wall-bounded turbulence. *Fluid Dyn. Res.* **51**, 011408.

EGGELS, J.G.M., UNGER, F., WEISS, M.H., WESTERWEEL, J., ADRIAN, R.J., FRIEDRICH, R. & NIEUWSTADT, F.T.M. 1994 Fully developed turbulent pipe flow: a comparison between direct numerical simulation and experiment. *J. Fluid Mech.* **268**, 175–210.

EL KHOURY, G.K., SCHLATTER, P., NOORANI, A., FISCHER, P.F., BRETHOUWER, G. & JOHANSSON, A.V. 2013 Direct numerical simulation of turbulent pipe flow at moderately high Reynolds numbers. *Flow Turbul. Combust.* **91** (3), 475–495.

FELDMANN, D., BAUER, C. & WAGNER, C. 2018 Computational domain length and Reynolds number effects on large-scale coherent motions in turbulent pipe flow. *J. Turbul.* **19** (3), 274–295.

FIORINI, T. 2017 Turbulent pipe flow – high resolution measurements in CICLoPE. PhD thesis, Universitá di Bologna.

FURUICHI, N., TERAO, Y., WADA, Y. & TSUJI, Y. 2015 Friction factor and mean velocity profile for pipe flow at high Reynolds numbers. *Phys. Fluids* **27** (9), 095108.

FURUICHI, N., TERAO, Y., WADA, Y. & TSUJI, Y. 2018 Further experiments for mean velocity profile of pipe flow at high Reynolds number. *Phys. Fluids* **30** (5), 055101.

GUALA, M., HOMMEMA, S.E. & ADRIAN, R.J. 2006 Large-scale and very-large-scale motions in turbulent pipe flow. *J. Fluid Mech.* **554**, 521–542.

HELLSTRÖM, L.H.O., SINHA, A. & SMITS, A.J. 2011 Visualizing the very-large-scale motions in turbulent pipe flow. *Phys. Fluids* **23** (1), 011703.

HINZE, J.O. 1975 *Turbulence*. McGraw-Hill.

HOYAS, S. & JIMÉNEZ, J. 2006 Scaling of the velocity fluctuations in turbulent channels up to $Re_\tau = 2003$. *Phys. Fluids* **18** (1), 011702.

HOYAS, S., OBERLACK, M., ALCÁNTARA-ÁVILA, F., KRAHEBERGER, S.V. & LAUX, J. 2022 Wall turbulence at high friction Reynolds numbers. *Phys. Rev. Fluids* **7** (1), 014602.

HULTMARK, M., VALLIKIVI, M., BAILEY, S.C.C. & SMITS, A.J. 2012 Turbulent pipe flow at extreme Reynolds numbers. *Phys. Rev. Lett.* **108**, 094501.

HUSSAIN, A.K.M.F. & REYNOLDS, W.C. 1975 Measurements in fully developed turbulent channel flow. *Trans. ASME J. Fluids Engng* **97** (4), 568–578.

HUTCHINS, N. & MARUSIC, I. 2007 Evidence of very long meandering features in the logarithmic region of turbulent boundary layers. *J. Fluid Mech.* **579**, 1–28.

HWANG, J., LEE, J., SUNG, H.J. & ZAKI, T.A. 2016 Inner–outer interactions of large-scale structures in turbulent channel flow. *J. Fluid Mech.* **790**, 128–157.

JIMÉNEZ, J. 2012 Cascades in wall-bounded turbulence. *Annu. Rev. Fluid Mech.* **44**, 27–45.

JIMÉNEZ, J., HOYAS, S., SIMENS, M.P. & MIZUNO, Y. 2010 Turbulent boundary layers and channels at moderate Reynolds numbers. *J. Fluid Mech.* **657**, 335–360.

JIMÉNEZ, J. & MOSER, R.D. 2007 What are we learning from simulating wall turbulence? *Phil. Trans. R. Soc.* A **365** (1852), 715–732.

KIM, J. 2011 Physics and control of wall turbulence for drag reduction. *Phil. Trans. R. Soc. Lond.* A **369** (1940), 1396–1411.

KIM, K.C. & ADRIAN, R.J. 1999 Very large-scale motion in the outer layer. *Phys. Fluids* **11** (2), 417–422.

KIM, J., MOIN, P. & MOSER, R. 1987 Turbulence statistics in fully developed channel flow at low Reynolds number. *J. Fluid Mech.* **177**, 133–166.

KLEWICKI, J.C. 2022 Bounded dissipation predicts finite asymptotic state of near-wall turbulence. *J. Fluid Mech.* **940**, F1.

LEE, M. & MOSER, R.D. 2015 Direct numerical simulation of turbulent channel flow up to $Re_\tau = 5200$. *J. Fluid Mech.* **774**, 395–415.

LEE, J.H. & SUNG, H.J. 2013 Comparison of very-large-scale motions of turbulent pipe and boundary layer simulations. *Phys. Fluids* **25** (4), 045103.

LOZANO-DURÁN, A. & JIMÉNEZ, J. 2014 Effect of the computational domain on direct simulations of turbulent channels up to $Re_\tau = 4200$. *Phys. Fluids* **26** (1), 011702.

LUCHINI, P. 2017 Universality of the turbulent velocity profile. *Phys. Rev. Lett.* **118** (22), 224501.

MARUSIC, I., BAARS, W.J. & HUTCHINS, N. 2017 Scaling of the streamwise turbulence intensity in the context of inner–outer interactions in wall turbulence. *Phys. Rev. Fluids* **2**, 100502.

MARUSIC, I., MATHIS, R. & HUTCHINS, N. 2010*a* Predictive model for wall-bounded turbulent flow. *Science* **329** (5988), 193–196.

MARUSIC, I., MCKEON, B.J., MONKEWITZ, P.A., NAGIB, H.M., SMITS, A.J. & SREENIVASAN, K.R. 2010*b* Wall-bounded turbulent flows at high Reynolds numbers: recent advances and key issues. *Phys. Fluids* **22** (6), 065103.

MARUSIC, I. & MONTY, J.P. 2019 Attached eddy model of wall turbulence. *Annu. Rev. Fluid Mech.* **51**, 49–74.

MARUSIC, I., MONTY, J.P., HULTMARK, M. & SMITS, A.J. 2013 On the logarithmic region in wall turbulence. *J. Fluid Mech.* **716**, R3.

MATHIS, R., HUTCHINS, N. & MARUSIC, I. 2009 Large-scale amplitude modulation of the small-scale structures in turbulent boundary layers. *J. Fluid Mech.* **628**, 311–337.

MCKEON, B.J., ZAGAROLA, M.V. & SMITS, A.J. 2005 A new friction factor relationship for fully developed pipe flow. *J. Fluid Mech.* **538**, 429–443.

MONTY, J.P., HUTCHINS, N., NG, H.C.H., MARUSIC, I. & CHONG, M.S. 2009 A comparison of turbulent pipe, channel and boundary layer flows. *J. Fluid Mech.* **632**, 431–442.

MONTY, J.P., STEWART, J.A., WILLIAMS, R.C. & CHONG, M.S. 2007 Large-scale features in turbulent pipe and channel flows. *J. Fluid Mech.* **589**, 147–156.

MOSER, R.D., KIM, J. & MANSOUR, N.N. 1999 Direct numerical simulation of turbulent channel flow up to $Re_\tau = 590$. *Phys. Fluids* **11** (4), 943–945.

NAGIB, H.M. & CHAUHAN, K.A. 2008 Variations of von Kármán coefficient in canonical flows. *Phys. Fluids* **20** (10), 101518.

NICKELS, T.B., MARUSIC, I., HAFEZ, S. & CHONG, M.S. 2005 Evidence of the k^{-1} law in a high-Reynolds-number turbulent boundary layer. *Phys. Rev. Lett.* **95** (7), 074501.

NIKURADSE, J. 1933 Strömungsgesetze in rauhen Rohren. *VDI Forsch.* **361**, 1.

OLIVER, T.A., MALAYA, N., ULERICH, R. & MOSER, R.D. 2014 Estimating uncertainties in statistics computed from direct numerical simulation. *Phys. Fluids* **26** (3), 035101.

ÖRLÜ, R. & SCHLATTER, P. 2011 On the fluctuating wall-shear stress in zero pressure-gradient turbulent boundary layer flows. *Phys. Fluids* **23** (2), 021704.

PERRY, A.E., HENBEST, S. & CHONG, M.S. 1986 A theoretical and experimental study of wall turbulence. *J. Fluid Mech.* **165**, 163–199.

PIROZZOLI, S., ROMERO, J., FATICA, M., VERZICCO, R. & ORLANDI, P. 2021 One-point statistics for turbulent pipe flow up to $Re_\tau \approx 6000$. *J. Fluid Mech.* **926**, A28.

POPE, S.B. 2000 *Turbulent Flows*. Cambridge University Press.

REZAEIRAVESH, S., VINUESA, R. & SCHLATTER, P. 2021 UQit: a Python package for uncertainty quantification (UQ) in computational fluid dynamics (CFD). *J. Open Source Software* **6** (60), 2871.

REZAEIRAVESH, S., XAVIER, D., VINUESA, R., YAO, J., HUSSAIN, F. & SCHLATTER, P. 2022 Estimating uncertainty of low- and high-order turbulence statistics in wall turbulence. In *12th International Symposium on Turbulence and Shear Flow Phenomena (TSFP12), Osaka, Japan*.

ROSENBERG, B.J., HULTMARK, M., VALLIKIVI, M., BAILEY, S.C.C. & SMITS, A.J. 2013 Turbulence spectra in smooth- and rough-wall pipe flow at extreme Reynolds numbers. *J. Fluid Mech.* **731**, 46–63.

SCHLATTER, P. & ÖRLÜ, R. 2010 Assessment of direct numerical simulation data of turbulent boundary layers. *J. Fluid Mech.* **659**, 116–126.

SCHOPPA, W. & HUSSAIN, F. 2002 Coherent structure generation in near-wall turbulence. *J. Fluid Mech.* **453**, 57–108.

SHE, Z.-S., CHEN, X. & HUSSAIN, F. 2017 Quantifying wall turbulence via a symmetry approach: a Lie group theory. *J. Fluid Mech.* **827**, 322–356.

SILLERO, J.A., JIMÉNEZ, J. & MOSER, R.D. 2013 One-point statistics for turbulent wall-bounded flows at Reynolds numbers up to $\delta^+ \approx 2000$. *Phys. Fluids* **25** (10), 105102.

SMITS, A.J., HULTMARK, M., LEE, M., PIROZZOLI, S. & WU, X. 2021 Reynolds stress scaling in the near-wall region of wall-bounded flows. *J. Fluid Mech.* **926**, A31.

SMITS, A.J., MCKEON, B.J. & MARUSIC, I. 2011*b* High-Reynolds number wall turbulence. *Annu. Rev. Fluid Mech.* **43**, 353–375.

SMITS, A.J., MONTY, J., HULTMARK, M., BAILEY, S.C.C., HUTCHINS, N. & MARUSIC, I. 2011*a* Spatial resolution correction for wall-bounded turbulence measurements. *J. Fluid Mech.* **676**, 41–53.

SREENIVASAN, K.R. 1989 The turbulent boundary layer. In *Frontiers in Experimental Fluid Mechanics* (ed. M. Gad-el-Hak), pp. 159–209. Springer.

TALAMELLI, A., PERSIANI, F., FRANSSON, J.H.M., ALFREDSSON, P.H., JOHANSSON, A.V., NAGIB, H.M., RÜEDI, J.-D., SREENIVASAN, K.R. & MONKEWITZ, P.A. 2009 CICLoPE – a response to the need for high Reynolds number experiments. *Fluid Dyn. Res.* **41** (2), 021407.

WALEFFE, F. 1997 On a self-sustaining process in shear flows. *Phys. Fluids* **9** (4), 883–900.

WILLERT, C.E., SORIA, J., STANISLAS, M., KLINNER, J., AMILI, O., EISFELDER, M., CUVIER, C., BELLANI, G., FIORINI, T. & TALAMELLI, A. 2017 Near-wall statistics of a turbulent pipe flow at shear Reynolds numbers up to 40 000. *J. Fluid Mech.* **826**, R5.

WILLIS, A.P. 2017 The Openpipeflow Navier–Stokes solver. *SoftwareX* **6**, 124–127.

WU, X., BALTZER, J.R. & ADRIAN, R.J. 2012 Direct numerical simulation of a 30*R* long turbulent pipe flow at $R^+ = 685$: large- and very large-scale motions. *J. Fluid Mech.* **698**, 235–281.

WU, X. & MOIN, P. 2008 A direct numerical simulation study on the mean velocity characteristics in turbulent pipe flow. *J. Fluid Mech.* **608**, 81–112.

YANG, X.I.A., HONG, J., LEE, M. & HUANG, X.L.D. 2021 Grid resolution requirement for resolving rare and high intensity wall-shear stress events in direct numerical simulations. *Phys. Rev. Fluids* **6** (5), 054603.

YANG, X.I.A. & LOZANO-DURÁN, A. 2017 A multifractal model for the momentum transfer process in wall-bounded flows. *J. Fluid Mech.* **824**.

YAO, J., CHEN, X. & HUSSAIN, F. 2018 Drag control in wall-bounded turbulent flows via spanwise opposed wall-jet forcing. *J. Fluid Mech.* **852**, 678–709.

ZAGAROLA, M.V. & SMITS, A.J. 1998 Mean-flow scaling of turbulent pipe flow. *J. Fluid Mech.* **373**, 33–79.